

RoboBEV: Towards Robust Bird’s Eye View Perception under Corruptions

Shaoyuan Xie¹ Lingdong Kong^{2,3} Wenwei Zhang^{2,4} Jiawei Ren⁴
Liang Pan⁴ Kai Chen² Ziwei Liu⁴✉

¹ Huazhong University of Science and Technology ² Shanghai AI Laboratory ³ National University of Singapore

⁴ S-Lab, Nanyang Technological University

shaoyuanxie@hust.edu.cn {konglingdong, zhangwenwei, chencai}@pjlab.org.cn {jiawei011, liang.pan, ziwei.liu}@ntu.edu.sg

Abstract

The recent advances in camera-based bird’s eye view (BEV) representation exhibit great potential for in-vehicle 3D perception. Despite the substantial progress achieved on standard benchmarks, the robustness of BEV algorithms has not been thoroughly examined, which is critical for safe operations. To bridge this gap, we introduce **RoboBEV**, a comprehensive benchmark suite that encompasses eight distinct corruptions, including Bright, Dark, Fog, Snow, Motion Blur, Color Quant, Camera Crash, and Frame Lost. Based on it, we undertake extensive evaluations across a wide range of BEV-based models to understand their resilience and reliability. Our findings indicate a strong correlation between absolute performance on in-distribution and out-of-distribution datasets. Nonetheless, there are considerable variations in relative performance across different approaches. Our experiments further demonstrate that pre-training and depth-free BEV transformation has the potential to enhance out-of-distribution robustness. Additionally, utilizing long and rich temporal information largely helps with robustness. Our findings provide valuable insights for designing future BEV models that can achieve both accuracy and robustness in real-world deployments.¹

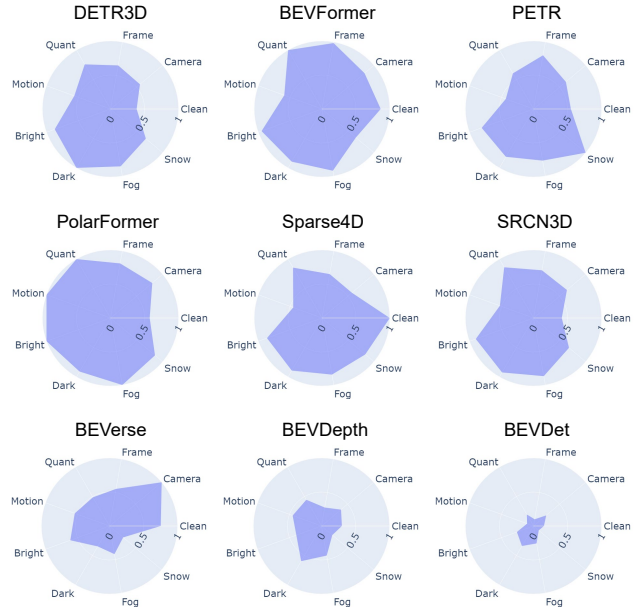


Figure 1. The radar charts of existing BEV detectors’ nuScenes Detection Score (NDS) [3] under eight corruption types. We observe diverse behaviors of different models even with competitive “clean” performance. The NDS is normalized across all the benchmarking BEV models to lie between 0.1 and 1.

1. Introduction

Deep neural network-based 3D perception methods have exhibited remarkable performance on various challenging benchmarks [19, 43, 13, 23, 42, 41, 16, 40, 48, 46]. The camera-based approaches [19, 43, 13, 23, 42, 41] have garnered significant attention in comparison to LiDAR-based methods [16, 40, 48, 46], owing to their low deployment cost, high computational efficiency, and dense semantic information. Moreover, building representations in the bird’s eye view (BEV) offers several benefits. Firstly, it allows for joint learning from multi-view images. Secondly, the

bird’s eye perspective provides a physics-interpretable way for information fusion from different sensors and timestamps [26]. Lastly, BEV output space is easily applicable in many downstream tasks, such as prediction and planning, which leads to significant improvements in performance for BEV-based perception frameworks.

Despite the remarkable progress achieved by recent BEV perception methods, their robustness against out-of-context scenarios remains inadequately understood. This is particularly concerning given that these methods are typically utilized in highly safety-critical systems (e.g., autonomous driving systems) in the real world. Generally, robustness can be divided into two categories: adversarial robustness [6] and robustness under natural corruptions [11]. Very

¹Code: <https://github.com/Daniel-xsy/RoboBEV>.



Figure 2. Corruption examples from the **RoboBEV** benchmark. **Left:** Corruption taxonomy. **Right:** Temporal corruptions. *Camera Crash* drop fixed set of images along timestamps; *Frame Lost* randomly drop frames along timestamps. More examples are in Appendix 9.3.

recently, Xie *et al.* conduct a comprehensive study on the adversarial robustness of camera-based 3D detection models [45], which measures the *worst-case* performance but is difficult to implement in real-world settings. Conversely, we aim to investigate the robustness of camera-based 3D perception algorithms under natural corruptions, which measures *average-case* performance that occurs frequently in reality.

In this work, to address the existing knowledge gap, we present a comprehensive benchmark dubbed **RoboBEV**. This benchmark evaluates the robustness of camera-based BEV perceptions against natural corruptions including exterior environments, interior sensors, and temporal factors. Specifically, the exterior environments include various light and weather conditions, which are simulated by incorporating *Brightness*, *Dark*, *Fog*, and *Snow* weathers. Additionally, the inputs may be corrupted by interior factors caused by sensors, such as motion and color distortions. To this end, we consider *Motion Blur* and *Color Quant* to simulate these settings. Moreover, we propose two novel corruptions in temporal space tailored for BEV-based temporal fusion strategies, namely *Camera Crash* and *Frame Lost*. The study involves a comprehensive investigation of diverse out-of-distribution corruption settings that are highly relevant to real-world autonomous driving applications.

Leveraging the proposed **RoboBEV** benchmark, we conduct an exhaustive analysis of 26 camera-based BEV perception models under 8 corruptions across 3 severities. The benchmark results, as illustrated in Figure 1, demonstrate that models that exhibit competitive performance on standard datasets differ significantly in their performance on corrupted data and different corruptions. We mainly observe the following results: (a) the absolute performances show a strong correlation with the performances under corruption. However, the relative robustness does not neces-

sarily increase as standard performance improves; (b) pre-training together with depth-free BEV transformation has great potential to enhance robustness; (c) utilizing long and rich temporal information largely helps with robustness. Our findings provide valuable insights for the design of future models to strive for better robustness under natural corruptions. The key contributions of this work are summarized as follows:

- To the best of our knowledge, we make the first attempt to introduce **RoboBEV** for a comprehensive benchmark and evaluation of the robustness of camera-based BEV perceptions under natural corruptions.
- We conduct exhaustive experiments to evaluate **26** existing camera-based BEV perception algorithms under **eight** corruptions across **three** severities.
- Our study provides an in-depth analysis of the factors that contribute to superior robustness under corruption scenarios, which sheds light on future model design.

2. Related Work

Camera-based Bird’s Eye View Perception. The existing BEV perception can be divided into two categories based on whether they perform depth estimation explicitly. Inspired by LSS [32], BEVDet [13] utilizes an extra depth estimation branch to perform the transform from perspective view to bird’s eye view (PV2BEV). BEVDepth [18] makes more accurate depth estimation via explicit depth supervision from point clouds and further improves the performance. BEVerse [47] proposes a unified framework for multi-task learning and achieving state-of-the-art performance. Another line of work performs PV2BEV without explicit depth estimation. Following DETR [5], DETR3D [43] and ORA3D [34] represent 3D objects as queries and perform

cross-attention via Transformer decoder. PETR [23] further improves performance by proposing 3D position-aware representations. BEVFormer [19] introduces temporal cross-attention to extract BEV features from multi-timestamps images. PolarFormer [14] explores predicting 3D targets in polar coordinates. Inspired by the success of Sparse RCNN [37], SRCN3D [36] and Sparse4D [20] introduce sparse proposals for feature aggregation. SOLOFusion [31] attempts to fuse more history information in temporal modeling. Despite these works showing competitive results on the standard datasets, it’s unclear how they behave in front of natural corruptions.

Robustness under Adversarial Attacks. Contemporary neural networks are prone to adversarial attacks, where a deliberately created perturbation added to the input can lead the network to produce incorrect predictions [38, 8, 28]. Adversarial examples have been extensively researched in various vision tasks, including classification [38, 8, 28, 27, 2, 22], detection [44, 21, 39, 4], and segmentation [44, 35]. These adversarial examples can be generated both in digital [38, 8, 28, 27, 2, 22, 44] and physical environments [35, 15, 4]. The recent study demonstrates that the 3D perception system tends to crash when exposed to adversarial examples, which could pose potential safety risks in the deployment stages [35, 4, 39]. While Xie *et al.* [45] conducts a comprehensive study of the adversarial robustness of camera-based detectors, we focus on natural corruptions, which are more likely to occur in the real world.

Robustness under Natural Corruptions. The evaluation of model robustness has garnered significant research attention. Various benchmarks have been proposed to evaluate the robustness of 2D image classification models, *e.g.*, ImageNet-C [11], ObjectNet [1], ImageNetV2 [33], ImageNet-A [12], and ImageNet-R [33]. ImageNet-C intentionally corrupts the “clean” ImageNet samples with simulated corruptions like compression loss and motion blur, while ObjectNet collects a test set with rich variations in rotation, background, and viewpoint. ImageNetV2 re-collects a test set following ImageNet’s protocol and assesses the performance gap due to the natural distribution shift. ImageNet-A and ImageNet-R benchmark the classifier’s robustness to natural adversarial examples and abstract visual renditions, respectively. Hendrycks *et al.* [10] notes the correlation between the robustness of synthetic corruptions and the improvement of real-world cases. However, there is a lack of comparable benchmarks to evaluate the out-of-distribution robustness of the 3D BEV perception models, which are commonly employed in safety-critical applications. In this work, we present the first effort to investigate the robustness of these models under natural corruptions.

3. RoboBEV Benchmark

3.1. Benchmark Design

We present *nuScenes-C* as our benchmark dataset, which is generated by corrupting the validation set of the nuScenes dataset [3]. We choose nuScenes since it has been widely utilized among almost all the recent BEV models. Our benchmark dataset comprises *eight* different corruptions, which include various exterior environments, interior sensor distortions, and the newly introduced temporal corruptions. Following the experimental protocol established in [11], we establish *three* different levels of corruption intensity (*i.e.*, easy, moderate, and hard) for each type of corruption. The severity levels are carefully determined to avoid significant performance drops that could undermine the conclusions’ reliability. Additionally, we incorporate variations within each severity level of corruption to augment the benchmark’s diversity.

3.2. Natural Corruptions

The corruption taxonomy is shown in Figure 2. Our first category of corruption involves diverse exterior environment conditions, such as lighting and extreme weather conditions. To simulate these situations, we introduce *Brightness*, *Dark*, *Fog*, and *Snow*. Since the majority of images in autonomous driving datasets are captured under mild meteorological conditions with temperate lighting, it is crucial to ensure that the perception system could perform well under different exterior conditions.

Secondly, sensor distortions are also prevalent in the real world. Images captured by cameras can easily become blurred at high moving speeds, and images can be quantized to reduce memory when deployed on devices with strict resource constraints. To simulate these scenarios, we incorporate *Motion Blur* and *Color Quantization*.

Lastly, we consider the case where cameras may crash or drop certain frames due to physical problems. We simulate this scenario by introducing the *Camera Crash* corruption, where we randomly discard images from a fixed set of cameras based on the corruption intensity. Additionally, we propose *Frame Lost*, where we randomly drop multiple cameras independently with the same probability at each timestamp, emulating situations where some frames are lost in consecutive time sequences. Figure 2 illustrates these procedures.

In addition, we conduct an analysis of the pixel histogram. It is worth noting that while *Motion Blur* incurs the least amount of pixel distribution shift, it results in a significant reduction in performance. Further experimental results are provided in Section 4. For more visualization results, please refer to Appendix 10.1.

Table 1. BEV model calibration. **Pretrain**: model initialized from pretrained FCOS3D [41] checkpoint; **Temporal**: model utilizes temporal information; **Depth**: model with explicit depth estimation branch used in the pipeline; **CBGS**: model uses the class-balanced group-sampling training strategy [49]. **Bold**: Best in the category. Underline: Second best in the category.

Model	Pretrain	Temporal	Depth	CBGS	Backbone	BEV Encoder	Image Size	NDS \uparrow	mCE (%) \downarrow	mRR (%) \uparrow
DETR3D [43]	✓				ResNet	Attention	1600 × 900	0.4224	100.00	70.77
DETR3D _{CBGS} [43]	✓			✓	ResNet	Attention	1600 × 900	0.4341	99.21	70.02
BEVFormer (small) [19]	✓	✓			ResNet	Attention	1280 × 720	<u>0.4787</u>	101.23	59.07
BEVFormer-S (small) [19]	✓				ResNet	Attention	1280 × 720	0.2622	114.43	76.87
BEVFormer (base) [19]	✓	✓			ResNet	Attention	1600 × 900	0.5174	<u>97.97</u>	60.40
BEVFormer-S (base) [19]	✓				ResNet	Attention	1600 × 900	0.4129	101.87	69.33
PETR (r50) [23]					ResNet	Attention	1408 × 512	0.3665	111.01	61.26
PETR (vov) [23]	✓				VoVNet-V2	Attention	1600 × 640	0.4550	100.69	65.03
ORA3D [34]	✓				ResNet	Attention	1600 × 900	0.4436	99.17	68.63
PolarFormer (r101) [14]	✓				ResNet	Attention	1600 × 900	0.4602	96.06	<u>70.88</u>
PolarFormer (vov) [14]	✓				VoVNet-V2	Attention	1600 × 900	0.4558	98.75	67.51
SRCN3D (r101) [36]	✓				ResNet	CNN + Attn.	1600 × 900	0.4286	99.67	70.23
SRCN3D (vov) [36]	✓				VoVNet-V2	CNN + Attn.	1600 × 900	0.4205	102.04	67.95
Sparse4D (r101) [20]	✓	✓			ResNet	CNN + Attn.	1600 × 640	0.5438	100.01	55.04
BEVDet (r50) [13]			✓	✓	ResNet	CNN	704 × 256	0.3770	115.12	51.83
BEVDet (r101) [13]			✓	✓	ResNet	CNN	704 × 256	0.3877	113.68	53.12
BEVDet (r101) [13]	✓		✓	✓	ResNet	CNN	704 × 256	0.3780	112.80	56.35
BEVDet (tiny) [13]			✓	✓	SwinTrans	CNN	704 × 256	0.4037	116.48	46.26
BEVDepth (r50) [18]			✓	✓	ResNet	CNN	704 × 256	0.4058	110.02	56.82
BEVerse (swin-t) [47]		✓	✓	✓	SwinTrans	CNN	704 × 256	0.4665	110.67	48.60
BEVerse-S (swin-t) [47]			✓	✓	SwinTrans	CNN	704 × 256	0.1603	137.25	28.24
BEVerse (swin-s) [47]		✓	✓	✓	SwinTrans	CNN	1408 × 512	<u>0.4951</u>	117.82	49.57
BEVerse-S (swin-s) [47]			✓	✓	SwinTrans	CNN	1408 × 512	0.2682	132.13	29.54
SOLOFusion (short) [31]		✓	✓		ResNet	CNN	704 × 256	0.3907	108.68	61.45
SOLOFusion (long) [31]		✓	✓		ResNet	CNN	704 × 256	0.4850	<u>97.99</u>	<u>64.42</u>
SOLOFusion (fusion) [31]		✓	✓	✓	ResNet	CNN	704 × 256	0.5381	92.86	64.53

3.3. Robustness Metrics

We follow the official nuScenes metric [3] to calculate robustness metrics on the *nuScenes-C* dataset. We report nuScenes Detection Score (NDS) and mean Average Precision (mAP), along with mean Average Translation Error (mATE), mean Average Scale Error (mASE), mean Average Orientation Error (mAOE), mean Average Velocity Error (mAVE) and mean Average Attribute Error (mAAE).

To better compare the robustness among different BEV detectors, we introduce two new metrics inspired by [11] based on NDS. The first metric is the mean corruption error (mCE), which is applied to measure the *relative robustness* of candidate models compared to the baseline model:

$$CE_i = \frac{\sum_{l=1}^3 (1 - NDS)_{i,l}}{\sum_{l=1}^3 (1 - NDS_{baseline})_{i,l}}, \quad mCE = \frac{1}{N} \sum_{i=1}^N CE_i, \quad (1)$$

where i denotes the corruption type and l is the severity level; N denotes the number of corruption types in our benchmark. To compare the *performance discrepancy* between *nuScenes-C* and the standard nuScenes dataset, we define a simple mean resilience rate (mRR) metric, which is calculated across three severity levels as follows:

$$RR_i = \frac{\sum_{l=1}^3 NDS_{i,l}}{3 \times NDS_{clean}}, \quad mRR = \frac{1}{N} \sum_{i=1}^N RR_i. \quad (2)$$

In our benchmark, we report both metrics for each candidate BEV algorithm and draw key analyses upon them.

4. Experiments

4.1. Experimental Setup

In our study, we use the official model configurations and public weight checkpoints provided by open-sourced codebases, whenever applicable; while we also train additional model variants with minimal modifications to conduct experiments under controlled settings. To ensure high consistency and reproducibility, we set a fixed random seed for all experiments. Furthermore, we report metrics for each corruption type by averaging over three severities. We adopt DETR3D [43] as our baseline for the mCE metric, considering its wide adoption as a state-of-the-art approach. Our code is built upon MMDetection3D codebase [7].

4.2. Main Benchmarking Results

In this study, we conduct a comprehensive benchmarking analysis of 26 existing BEV detectors on the *nuScenes-C* dataset. The main results of our experiments are presented in Tables 2 and 3. Our findings indicate that all models exhibit varying degrees of performance declines on the corruption set. We observed that *Bright*, which causes a much larger shift in pixel distribution than *Motion Blur*, resulted

Table 2. The **Corruption Error (CE)** of each BEV detector in our *RoboBEV* benchmark. **Bold**: Best in the category. **Blue** : Best in the row if improve upon baseline. **Yellow** : Worst in the row if decline upon baseline. †: distinguish pre-training version BEVDet.

Model	NDS ↑	mCE (%) ↓	Camera	Frame	Quant	Motion	Bright	Dark	Fog	Snow
DETR3D [43]	0.4224	100.00	100.00	100.00	100.00	100.00	100.00	100.00	100.00	100.00
DETR3DCBGs [43]	0.4341	99.21	98.15	98.90	99.15	101.62	97.47	100.28	98.23	99.85
BEVFormer (small) [19]	0.4787	102.40	101.23	101.96	98.56	101.24	104.35	105.17	105.40	101.29
BEVFormer (base) [19]	0.5174	97.97	95.87	94.42	95.13	99.54	96.97	103.76	97.42	100.69
PETR (r50) [23]	0.3665	111.01	107.55	105.92	110.33	104.93	119.36	116.84	117.02	106.13
PETR (vov) [23]	0.4550	100.69	99.09	97.46	103.06	102.33	102.40	106.67	103.43	91.11
ORA3D [34]	0.4436	99.17	97.26	98.03	97.32	100.19	98.78	102.40	99.23	100.19
PolarFormer (r101) [14]	0.4602	96.06	96.16	97.24	95.13	92.37	94.96	103.22	94.25	95.17
PolarFormer (vov) [14]	0.4558	98.75	96.13	97.20	101.48	104.32	95.37	104.78	97.55	93.14
SRCN3D (r101) [36]	0.4286	99.67	98.77	98.96	97.93	100.71	98.80	102.72	99.54	99.91
SRCN3D (vov) [36]	0.4205	102.04	99.78	100.34	105.13	107.06	101.93	107.10	102.27	92.75
Sparse4D (r101) [20]	0.5438	100.01	99.80	99.91	98.05	102.00	100.30	103.83	100.46	95.72
BEVDet (r50) [13]	0.3770	115.12	105.22	109.19	111.27	108.18	123.96	123.34	123.83	115.93
BEVDet (tiny) [13]	0.4037	116.48	103.50	106.61	113.18	107.26	130.19	131.83	124.01	115.25
BEVDet (r101) [13]	0.3877	113.68	103.32	107.29	109.25	105.40	124.14	123.12	123.28	113.64
BEVDet (r101†) [13]	0.3780	112.80	105.84	108.68	101.99	100.97	123.39	119.31	130.21	112.04
BEVDepth (r50) [18]	0.4058	110.02	103.09	106.26	106.24	102.02	118.72	114.26	116.57	112.98
BEVerse (swin-t) [47]	0.4665	110.67	95.49	94.15	108.46	100.19	122.44	130.40	118.58	115.69
BEVerse (swin-s) [47]	0.4951	107.82	92.93	101.61	105.42	100.40	110.14	123.12	117.46	111.48
SOLOFusion (short) [31]	0.3907	108.68	104.45	105.53	105.47	100.79	117.27	110.44	115.01	110.47
SOLOFusion (long) [31]	0.4850	97.99	95.80	101.54	93.83	89.11	100.00	99.61	98.70	105.35
SOLOFusion (fusion) [31]	0.5381	92.86	86.74	88.37	87.09	86.63	94.55	102.22	90.67	106.64

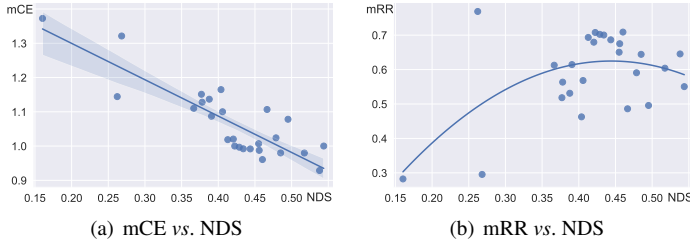


Figure 3. The performance on *nuScenes-C* is improved as the performance on the “clean” *nuScenes* [3] dataset. The relation of absolute performance is close to linear. However, when considering the relative performance, the mRR metric is more randomly distributed without a clear trend to increase.

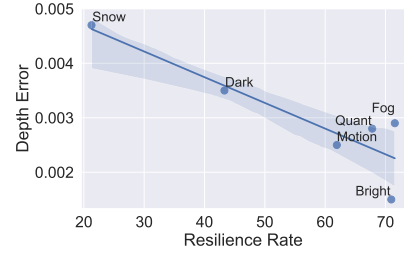


Figure 4. Depth estimation error vs. Resilience Rate. We observe strong correlations where large depth estimation errors under *Snow* and *Dark* tend to cause drastic performance drops.

in the smallest performance drop. For most of the models, the resilience rate of *Bright* remains the highest.

We notice a strong correlation of the absolute performances between *nuScenes-C* and the “clean” dataset. Specifically, BEV detectors that perform well on the standard dataset are also likely to perform better on the out-of-distribution dataset, as illustrated in Figure 3(a). However, a closer examination of the results revealed a more complex situation. Models with similar performance on the “clean” dataset exhibit diverse robustness under different types of corruption. For example, BEVerse (swin-s) [47] demonstrates significantly improved robustness in *Camera Crash* compared to the baseline, while PETR (vov) [23] performs well in *Snow* weather. However, both models struggle to make accurate predictions under *Dark* conditions.

We further find that resilience rates under corruptions confront the risk of decreasing. Superior performances on

the standard dataset do not necessarily lead to better resilience rates. While the mCE metric reveals a linear relationship between absolute performance on the *nuScenes* dataset and the *nuScenes-C* dataset, the mRR metric shows large variations among models exhibiting competitive standard performance, suggesting that some models may overfit the *nuScenes* dataset and struggle to generalize well to the *nuScenes-C* dataset.

This is exemplified by Sparse4D [20] outperforming DETR3D [43] on the “clean” dataset while having lower mRR metrics for all corruption types. Furthermore, we observe that DETR3D exhibits the most robust performance under *Dark* conditions, while BEVerse (swin-t) with better “clean” performance only achieves a relative performance of approximately 12% under dark lighting conditions. Therefore, we suggest that benchmarking state-of-the-art models from multiple perspectives is critical to com-

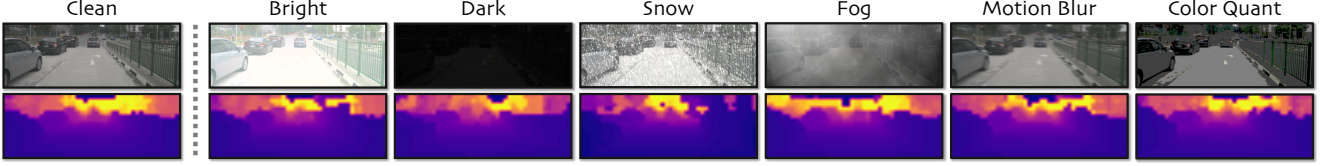


Figure 5. Depth estimation results of BEVDepth [18] under different corruptions. The results exhibit a different sensitivity for each type.

Table 3. The **Resilience Rate (RR)** of each BEV detector in our *RoboBEV* benchmark. **Bold**: best within the category. **Blue**: Best across category. †: distinguish pre-training version BEVDet.

Model	NDS	mRR (%) ↑	Camera	Frame	Quant	Motion	Bright	Dark	Fog	Snow
DETR3D [43]	0.4224	70.77	67.68	61.65	75.21	63.00	94.74	65.96	92.61	45.29
DETR3D _{CBGS} [43]	0.4341	70.02	68.90	61.85	74.52	58.56	95.69	63.72	92.61	44.34
BEVFormer (small) [19]	0.4787	59.07	57.89	51.37	68.41	53.69	78.15	50.41	74.85	37.79
BEVFormer (base) [19]	0.5174	60.40	60.96	58.31	67.82	52.09	80.87	48.61	78.64	35.89
PETR (r50) [23]	0.3665	61.26	63.30	59.10	67.45	62.73	77.52	42.86	78.47	38.66
PETR (vov) [23]	0.4550	65.03	64.26	61.36	65.23	54.73	84.79	50.66	81.38	57.85
ORA3D [34]	0.4436	68.63	68.87	61.99	75.74	59.67	91.86	58.90	89.25	42.79
PolarFormer (r101) [14]	0.4602	70.88	68.08	61.02	76.25	69.99	93.52	55.50	92.61	50.07
PolarFormer (vov) [14]	0.4558	67.51	68.78	61.67	67.49	51.43	93.90	53.55	89.10	54.15
SRCN3D (r101) [36]	0.4286	70.23	68.76	62.55	77.41	60.87	95.05	60.43	91.93	44.80
SRCN3D (vov) [36]	0.4205	67.95	68.37	61.33	67.23	50.96	92.41	54.08	89.75	59.43
Sparse4D(r101) [20]	0.5438	55.04	52.83	48.01	60.87	46.23	73.26	46.16	71.42	41.54
BEVDet (r50) [13]	0.3770	51.83	65.94	51.03	63.87	54.67	68.04	29.23	65.28	16.58
BEVDet (tiny) [13]	0.4037	46.26	64.63	52.39	56.43	52.71	54.27	12.14	60.69	16.84
BEVDet (r101) [13]	0.3877	53.12	67.63	53.26	65.67	58.42	65.88	28.84	64.35	20.89
BEVDet (r101†) [13]	0.3780	56.35	64.60	51.90	80.45	68.52	68.76	36.85	54.84	24.84
BEVDepth (r50) [18]	0.4058	56.82	65.01	52.76	67.79	61.93	70.95	43.30	71.54	21.27
BEVerse (swin-t) [47]	0.4665	48.60	68.19	65.10	55.73	56.74	56.93	12.71	59.61	13.80
BEVerse (swin-s) [47]	0.4951	49.57	67.95	50.19	56.70	53.16	68.55	22.58	57.54	19.89
SOLOFusion (short) [31]	0.3907	61.45	65.04	56.18	71.77	66.62	75.92	52.03	76.73	27.28
SOLOFusion (long) [31]	0.4850	64.42	65.13	51.34	74.19	71.34	82.52	58.02	82.29	30.52
SOLOFusion (fusion) [31]	0.5381	64.53	70.73	64.37	75.41	67.68	80.45	48.80	83.26	25.57

prehensively evaluate their performance.

To further investigate the behavior of the model’s robustness, we break down BEV detectors into various components, namely, training strategies (e.g., FCOS3D [41] pre-training and CBGS [49] resampling strategy for addressing unbalanced classes), model architectures (e.g., backbone), and approach pipelines (e.g., temporal cue learning and depth estimation). The results of this analysis are in Table 1.

Specifically, we focus on FCOS3D [41] pre-training and CBGS [49] resampling strategy, as they are commonly utilized in these approaches and have demonstrated effectiveness in improving the performance of the “clean” dataset.

4.3. Camera-LiDAR Fusion

Apart from building BEV representations only from image inputs, BEVFusion [25] extracts a shared BEV space to fuse features from both image and point clouds. We consider the settings where the cameras are affected while the LiDAR works well, which are common happened in the real world. For instance, the capture process of point clouds is not disturbed by the lighting conditions but the images are

of low quality in the dark. In terms of weather like *Snow* and *Fog*, which can add noise to both camera and LiDAR, we do not consider this setting in this work. The results are shown in Table 4. It’s interesting to notice that the multi-modality fusion model still keeps high performance even when the imaging modality is corrupted. The performance of the fusion model under most natural corruptions outperforms that of the LiDAR-based model. This reveals that multi-modality inputs can be complementary when one of them degenerates.

5. Further Analysis

5.1. Depth Estimation

Depth-free BEV transformations show better robustness. Prior works in this area can be classified into two categories based on how they exploit depth estimation. The first category, including works such as BEVDet [13], BEVDepth [18], and BEVerse [47], incorporates an explicit depth-estimation branch in the pipeline. This is done because predicting 3D bounding boxes from monocular images is an ill-posed problem. These approaches first predict a per-pixel depth map, which is then used to map image

Table 4. NDS results of BEVFusion [25] under different input modalities. Since *Fog* and *Snow* can also affect the LiDAR sensors, we do not consider these two corruptions of the fusion model.

Camera	LiDAR	Clean	Camera	Frame	Quant	Motion	Bright	Dark	Fog	Snow
✓		0.4121	0.2777	0.2255	0.2763	0.2788	0.2902	0.1076	0.3041	0.1461
	✓	0.6928	—	—	—	—	—	—	—	—
✓	✓	0.7138	0.6963	0.6931	0.7044	0.6977	0.7018	0.6787	—	—

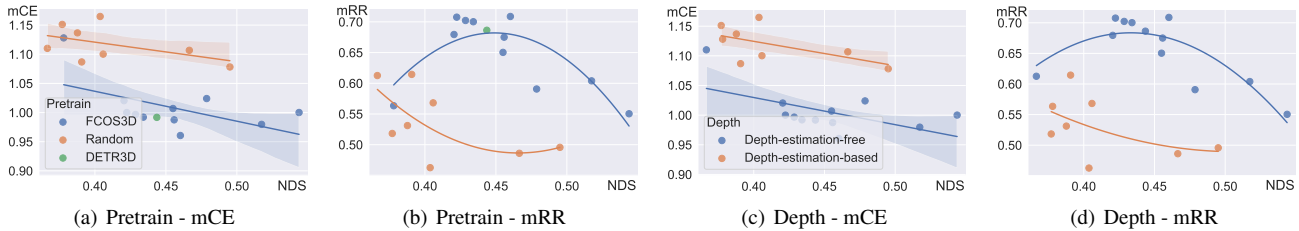


Figure 6. Pre-training strategies together with depth-free bird’s eye view transformation provide the models with better robustness. We do not consider SOLOFusion [31] long-term fusion here since it utilizes 16 frames, which is much larger than other methods.

features to corresponding 3D locations. Subsequently, they predict 3D targets in the bird’s-eye view (BEV) perspective by aggregating BEV features in a bottom-up fashion [43].

The second category of works uses pre-defined object queries [19, 43] or sparse proposals [20, 36] to index 2D features in a top-down manner. These two distinct designs demonstrate competitive performance on “clean” data, and we expand the analysis by evaluating their performance on out-of-distribution datasets. Our analysis reveals that depth-based approaches suffer from severe performance degradation when exposed to corrupted images as shown in Figure 6(c) and 6(d). The observed degradation could be due to inaccurate depth estimation, as illustrated in Figure 5.

Moreover, we undertake a comparative study to evaluate the intermediate depth estimation results of BEVDepth [18] under corruptions. To this end, we compute the mean square error (MSE) between “clean” inputs and corrupted inputs. Our findings indicate an explicit correlation between vulnerability and depth estimation error, as presented in Figure 4. Specifically, *Snow* and *Dark* corruptions significantly affect accurate depth estimation, leading to the largest performance drop. These results provide further support for our conclusion that the performance of depth-based approaches can suffer significantly if the depth estimation is not accurate enough.

5.2. Pre-Training

Pre-training improves robustness across a wide range of semantic corruptions while does not help with temporal corruptions. In recent years, pre-training has emerged as a promising technique for enhancing the performance of computer vision models across various tasks. In the context of 3D detection, it is common to use the FCOS3D [41] weights as initialization for the ResNet backbone. FCOS3D employs a depth weight of 0.2 for stable training, which is

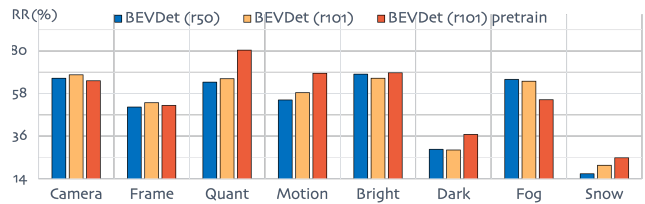


Figure 7. Resilience rate comparisons of BEVDet [13] with and without pre-training. The higher the better.

then switched to 1 for fine-tuning, as described in [41]. Alternatively, the VoVNet-V2 [17] backbone is first trained on the DDAD15M [9] dataset for depth estimation and then fine-tuned on the nuScenes train set for detection. These two pre-training strategies can be categorized as semantic and depth pre-training, respectively.

The effectiveness of these strategies for improving model robustness is illustrated in Figure 6(a) and Figure 6(b), where models utilize pre-training largely outperform those not. For controlled comparison, we re-implement the BEVDet (r101) model using the FCOS3D checkpoint as initialization. Our results, presented in Figure 7, show that pre-training can significantly improve mRR across a wide range of corruptions (except *Fog*) even if it has lower “clean” NDS (0.3780 vs. 0.3877). Specifically, under *Color Quant*, *Motion Blur*, and *Dark* corruptions, the mRR metric improves by 22.5%, 17.2%, and 27.8%, respectively. It’s worth noting that pre-training mainly improves most semantic corruptions and doesn’t improve temporal corruptions.

Even though, the pre-trained BEVDet still largely lags behind those depth-free counterparts. Therefore, pre-training together with the depth-free bird’s eye view transformation provides models with strong robustness.

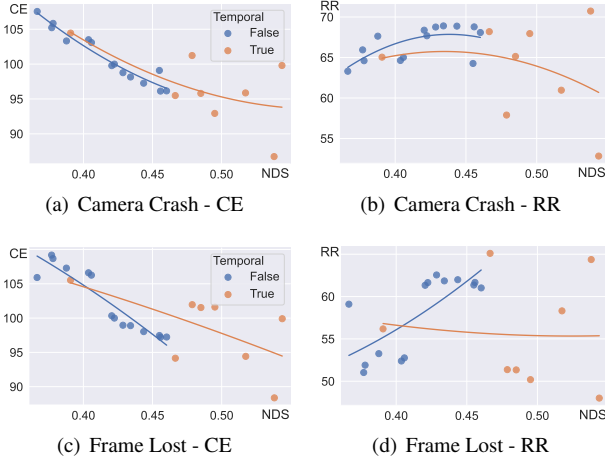
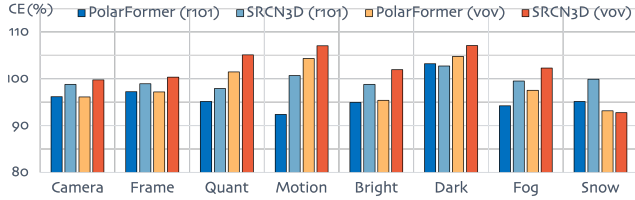
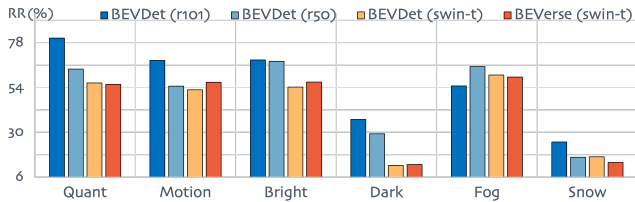


Figure 8. Not all the models with temporal fusion exhibit better robustness under *Camera Crash* and *Frame Lost*. However, they have the potential since the lowest mCE metric models are always those that utilize temporal information.



(a) ResNet vs. VoVNet-V2. Since the two versions have similar “clean” performances, we compare the absolute corruption error (the lower the better).



(b) ResNet vs. SwinTransformer. Since the models have different “clean” performances, we compare the relative resilience rate (the higher the better).

Figure 9. Comparisons of backbones under different corruptions.

5.3. Temporal Fusion

Temporal fusion has the potential to yield better absolute performance under corruptions. Fusing longer temporal information largely helps with robustness. In the context of autonomous driving, accurately estimating the velocity of moving objects based on a single-frame input is considerably challenging. Therefore, leveraging temporal cues to better perceive the surrounding environment is crucial for vision systems. Previous studies have proposed several approaches to learning effective temporal cues. In this investigation, we analyze whether temporal information can alleviate the impact of corrupted images. To this end, we choose BEVFormer [19] and BEVerse [47] for examination since both have single-frame and multi-frame versions,

enabling us to examine the influence of temporal information solely. Our experimental findings reveal that the use of multi-frame information substantially enhances the robustness of both the mCE and mRR metrics for BEVerse. For instance, the BEVerse Small improves from 132.12 to 117.82 on mCE and from 29.54 to 49.57 on mRR. However, for BEVFormer, the temporal cross-attention operation enhances the mCE metric but deteriorates the mRR metric from 69.33 to 60.40. We conjecture this might be caused by accumulation errors inside the history BEV features since BEVFormer stores the history information inside and update it on-the-fly while BEVerse consumes a fixed-size temporal window. For SOLOFusion [31], the RR metric of its long-only version outperforms its short-only counterpart on a wide range of corruption types, which indicates the great potential of utilizing longer temporal information.

We are particularly interested in examining how models utilizing temporal information perform under temporal corruptions. We find SOLOFusion which fuses wider and richer temporal information performs extremely well compared to its short-only and long-only versions. In terms of *Camera Crash*, the short-only and long-only versions have close resilience rate performance (65.04 vs. 65.13). However, the fusion version improves to 70.73, which is the highest among all the candidate models. Similarly, the fusion version improves the resilience rate by almost 10% compared to the other two versions under *Frame Lost* corruption.

Surprisingly, we further find that not all models with temporal fusion exhibit better robustness under *Camera Crash* and *Frame Lost*. The robustness is highly correlated to how to fuse history frames and how many frames are used, which emphasizes the importance of evaluating temporal fusion strategies from wider perspectives. The results can be seen in Figure 8. Nonetheless, temporal fusion remains a potential method to enhance temporal robustness since the models with the lowest Corruption Error (or the highest Resilience Rate) are consistently those that utilize temporal information.

5.4. Backbone

The Swin Transformer is more vulnerable towards the lighting changings; VoVNet-V2 is more robust against Snow while ResNet shows better robustness across a wide range of corruptions. It is noteworthy that various backbones demonstrate distinct responses to corruptions. PolarFormer [14] and SRCN3D [36], each having two backbone versions (i.e., ResNet and VoVNet-V2 [17]), exhibit similar standard performance. Nevertheless, ResNet-based detectors exhibit consistently superior robustness across a wide range of corruptions. For example, PolarFormer (r101) and SRCN3D (r101) demonstrate consistent improvements in the *Color Quant*, *Motion*, *Dark*, and *Fog*, as illustrated in

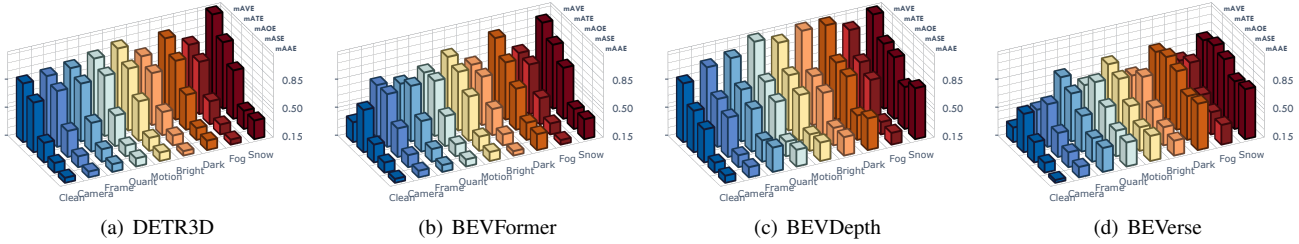


Figure 10. The detailed 3D detection metrics (mAVE, mATE, mAOE, mASE, and mAAE) reported on *nuScenes-C* other than NDS.

Figure 9(a). Conversely, the VoVNet-V2 [17] backbone consistently exhibits better robustness under *Snow* corruptions.

Moreover, Swin Transformer [24] based BEVDet demonstrates significant vulnerability towards changes in lighting conditions (*e.g.*, *Bright* and *Dark*). A clear comparison can be found between the ResNet-based BEVDet and the Swin-based BEVDet as shown in Figure 9(b). Additionally, the Swin-based BEVerse shows similar vulnerability towards these two corruptions, further supporting this conclusion.

5.5. Detailed nuScenes Metrics

The velocity prediction error significantly increases under corruptions, even for models with temporal fusion. The attribution and scale errors vary among models. The study primarily presents the NDS metrics, while additional detailed information regarding the model’s robustness can be found in Figure 10. It is observed that models employing temporal information have significantly lower mAVE metrics than those without such incorporation (*e.g.*, BEVFormer [19] and BEVerse [47]). However, in the presence of corrupted images, even under mild illumination conditions, the velocity prediction error significantly increases. Notably, the *Motion Blur* corruption also adversely affects the velocity predictions for BEVFormer and BEVerse, as shown in Figure 10(b) and 10(d). This highlights the vulnerability of models, which are even equipped with temporal information, in evaluating velocity under corrupted images.

Furthermore, attribution and scale errors show considerable variations across different models. For depth-free approaches, the errors of these metrics remain consistent, whereas there is a notable disparity for depth-based approaches. These findings further emphasize the vulnerability of depth-based approaches to corruptions.

6. Conclusions

In this work, we introduce the *RoboBEV* benchmark by utilizing a corpus of eight diverse natural corruptions to create the *nuScenes-C* dataset, which is used to assess the out-of-distribution robustness of camera-only BEV perception approaches. Exhaustive experiments are conducted to

investigate the factors that impact the model’s robustness. We hope the findings of this study provide valuable insights for designing future models that can achieve better out-of-distribution robustness.

7. Potential Limitations

Despite the eight distinct corruptions we introduce, they still cannot cover all the out-of-distribution contexts in real-world applications due to their unpredictable complexity. Additionally, we mainly analyze coarse-grained designs between models (*e.g.*, depth estimation) since it is considerably non-trivial to identify the trade-off between fine-grained network architecture designs (*e.g.*, the difference between SRCN3D and Sparse4D, and the different temporal fusion strategies for BEVFormer and BEVerse).

Appendix

In this appendix, we supplement the following materials to better support the findings and conclusions in the main body of this paper:

- Section 8 includes more details about the corruption setting, severity level, and model training.
- Section 9 provides the full *RoboBEV* benchmark results and some visualization results.
- Section 10 covers additional analyses of the experimental results in our benchmark.
- Section 11 acknowledges the public resources used during the course of this work.

8. Additional Implementation Details

8.1. Corruption Definition

We follow the severity protocol (*i.e.*, from severity 1 to 5) setting in ImageNet-C [11]. We choose the severity carefully to avoid drastic performance degeneration, which might impede us from drawing reliable conclusions. The details can be seen in Table 5.

For *Camera Crash*, we first randomly choose a set of cameras, and the number of the dropped cameras is equal to

the severity (*e.g.*, from one to five). In terms of *Frame Lost*, we randomly drop each camera with an identical probability at every single input frame in Equation 3.

$$p_{\text{drop}} = \text{severity} \times \frac{1}{6}. \quad (3)$$

The *Camera Crash* corruption evaluates the model’s behaviors when images from certain viewpoints are continuously lost, while the *Frame Lost* evaluates whether the model can make predictions by utilizing the last frame from the same sensors.

Table 5. The definition of corruption severity in *RoboBEV*, with a mapping to the severity protocol in defined in ImageNet-C [11].

Corruption	Easy	Moderate	Hard
Motion Blur	2	4	5
Color Quant	1	2	3
Bright	2	4	5
Dark	2	3	4
Fog	2	4	5
Snow	1	2	3
Camera Crash	2	4	5
Frame Lost	2	4	5

8.2. Re-Implementation

We re-implement the BEVDet (r101) [13], PolarFormer (vov) [14], and SRCN3D (vov) [36] models. For BEVDet (r101), we keep the input resolution the same as BEVDet(r50) for a fair comparison. Although this leads to lower results than the official report [13], we focus more on the robustness metric and draw meaningful conclusions rather than better performance on nuScenes [3] dataset.

The original PolarFormer (vov) and SRCN3D (vov) are initialized from DD3D [30] checkpoint, which uses nuScenes *trainval* set for training. This causes information leakage since the nuScenes-C dataset is corrupted from the nuScenes validation set. For fair comparisons, we re-implement these two models without modification but use the FCOS3D [41] model as initialization. The VoVNet-V2 [17] version FCOS3D models are first trained with depth estimation on the DDAD15M [9] dataset and then fine-tuned on the nuScenes train set.

9. Additional Experimental Results

In this section, we provide the full evaluation results of benchmarked models in the *RoboBEV* benchmark.

9.1. Map Segmentation

We further consider BEV-based map segmentation tasks. The results can be seen in Table 6. We use setting 1 as mentioned in [29] to report the Intersection over Union (IoU) with a threshold of 0.4 of vehicle map-view segmentation results. The performance of BEV-based map segmentation

Cross-View-Transformer is also severely hampered by corruption such as *Frame Lost* and *Snow*.

9.2. Corruption Robustness

We attach the full results, including monocular FCOS3D [41], please refer to Tab. 7 to Tab. 33.

- DETR3D [43]: See Tab. 7 for the results of the standard model; see Tab. 8 for the results of DETR3D_{CBGS}.
- ORA3D [34]: See Tab. 17 for ORA3D model.
- BEVFormer [19]: Refer to Tab. 11 and Tab. 9 for models that turn on multi-frame inference and Tab. 12 and Tab. 10 for single-frame versions.
- PETR [23]: Table 13 and Table 14 show results of PETR (r50) and PETR (vov), respectively.
- PolarFormer [14]: Table 15 and Table 16 show results of PolarFormer (r101) and our re-implement PolarFormer (vov).
- SRCN3D [36]: See Tab. 27 and Tab. 28 for SRCN3D (r101) model and our re-implement SRCN3D (vov) model.
- Sparse4D [20]: See Tab. 29 for Sparse4D (r101) model.
- BEVDet [13]: Refer to Tab. 18 and Tab. 21 for official implement; for our ResNet101 version implement, see Tab. 19 and Tab. 20.
- BEVDepth [18]: See Tab. 22 for BEVDepth (r50) model.
- BEVerse [47]: See Tab. 25 and Tab. 23 for temporal models; see Tab. 24 and Tab. 26 for single-frame models.
- SOLOFusion [31]: See Tab. 30, 31, and 32.
- FCOS3D [41]: See Tab. 33.

9.3. More Visualization Results

We provide more visualization results of the *nuScenes-C* dataset, as shown in Figure 16. The prediction results of BEVFormer [19] under moderate level corruptions can be seen in Figure 13, 14 and 15.

10. Additional Analysis

10.1. Corruptions

We calculate the pixel distribution over 300 images sampled from the nuScenes dataset and visualize the pixel histograms shown in Figure 11. Interestingly, the *Motion Blur*

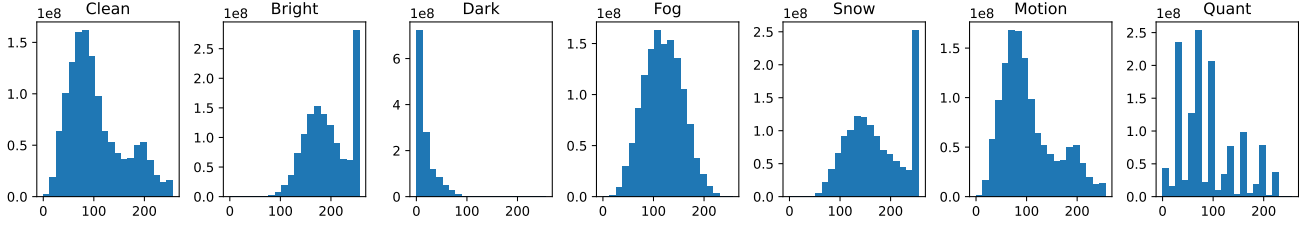


Figure 11. The pixel histogram of each corruption type in the *nuScenes-C* dataset.

Table 6. Map segmentation task results. The setting is the same as setting 1 mentioned in [29].

Model	Clean	Camera	Frame	Quant	Motion	Bright	Dark	Fog	Snow
CVT[29]	34.83	20.00	17.08	29.42	28.10	27.53	20.02	24.72	17.74

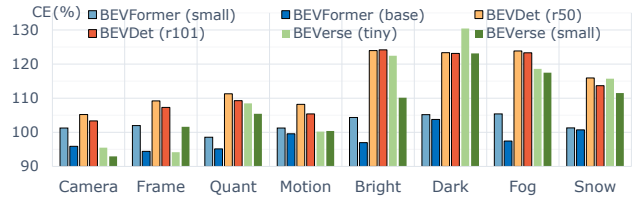
causes the least pixel distribution shifts while causing a relatively large performance drop. On the other hand, *Bright* shift the pixel distribution to higher values apparently and *Fog* makes fine-grained features more indistinct by shifting the pixel value more agminated. However, these two corruptions only lead to the smallest performance gap, which reveals that model robustness is not simply correlated with pixel distribution. Additionally, we visualize corruption error (resilience rate) vs. nuScenes detection score (NDS) under every single corruption as shown in Figure 18.

Temporal corruption. We observe a strong linear relationship between standard performance and performance on temporal corruptions as shown in Figure 18(a) and 18(c). Furthermore, We find models that utilize temporal information (e.g., BEVFormer) can output the prediction of a lost frame. However, these models still struggle to make predictions under *Camera Crash*, where consecutive frames of one camera are lost. The visualization results can be seen in Figure 14 and Figure 15. The *Camera Crash* and *Frame Lost* both drop images from the front left sensor. It’s interesting to see the model attempts to make predictions under *Frame Lost* while failing to output any prediction under *Camera Crash*.

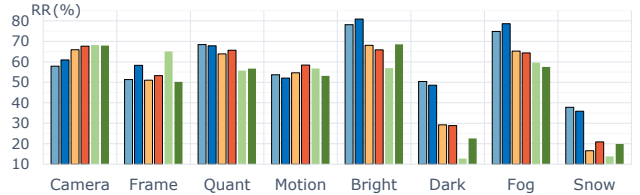
Motion and processing. However, in terms of other semantic corruption, models resent large variations. For example, the resilience rate of *Motion Blur* and *Color Quant* does not improve with the standard performance as shown in Figure 18(f) and 18(h). This reveals that the relative robustness does not necessarily improve as the standard performance and approaches to increase the generalization ability to sensor distortion are still unsolved in the context of 3D perception.

Weather and lighting condition. For weather and light corruptions, the resilience rate presents more promising results, where improvement on the standard dataset can ef-

fectively bring a better resilience rate. However, this also confronts the risk of decreasing as the NDS score surpasses 0.5. Performance under *Snow* corruption shows the greatest variation for models even under close standard performance. Thus, 3D perception algorithms are expected to be thoroughly examined from multiple perspectives (e.g., generalization ability to diverse environment conditions) to better understand their reliability.



(a) Corruption Error.



(b) Resilience Rate.

Figure 12. Comparisons of different backbone sizes.

10.2. Backbone Size

For most approaches, the final detection results will always improve if we enlarge the backbone network size (e.g., from ResNet50 to ResNet101). We hereby study how enlarging backbone network parameters influence model robustness. The comparison can be seen in Figure 12. We find enlarging backbone size can always bring lower corruption error. However, in terms of resilience rate (RR), the benefits of larger backbone sizes are limited. The ResNet101 version BEVFormer and BEVDet only outperform their

ResNet50 counterpart by a small margin. For BEVerse, the Swin-Small backbone shows better robustness towards *Bright*, *Dark*, and *Snow*.

11. Public Resources Used

We acknowledge the use of the following public resources, during the course of this work:

- nuScenes² CC BY-NC-SA 4.0
- nuScenes-devkit³ Apache License 2.0
- mmdetection3d⁴ Apache License 2.0
- imagecorruptions⁵ Apache License 2.0
- detr3d⁶ MIT License
- BEVFormer⁷ Apache License 2.0
- PolarFormer⁸ MIT License
- PETR⁹ Apache License 2.0
- SRCN3D¹⁰ MIT License
- BEVDet¹¹ Apache License 2.0
- BEVFusion¹² MIT License
- SOLOFusion¹³ Apache License 2.0
- Sparse4D¹⁴ Unknown
- BEVerse¹⁵ Unknown
- ora3d¹⁶ Unknown

²<https://www.nuscenes.org/nuscenes>.

³<https://github.com/nutonomy/nuscenes-devkit>.

⁴<https://github.com/open-mmlab/mmdetection3d>.

⁵<https://github.com/bethgelab/imagecorruptions>.

⁶<https://github.com/WangYueFt/detr3d>.

⁷<https://github.com/fundamentalvision/>

BEVFormer.

⁸<https://github.com/fudan-zvg/PolarFormer>.

⁹<https://github.com/megvii-research/PETR>.

¹⁰<https://github.com/synsin0/SRCN3D>.

¹¹<https://github.com/HuangJunJie2017/BEVDet>.

¹²<https://github.com/mit-han-lab/bevfusion>.

¹³<https://github.com/Divadi/SOLOFusion>.

¹⁴<https://github.com/linuxewu/Sparse4D>.

¹⁵<https://github.com/zhangyp15/BEVerse>.

¹⁶<https://github.com/anonymous2776/ora3d>.

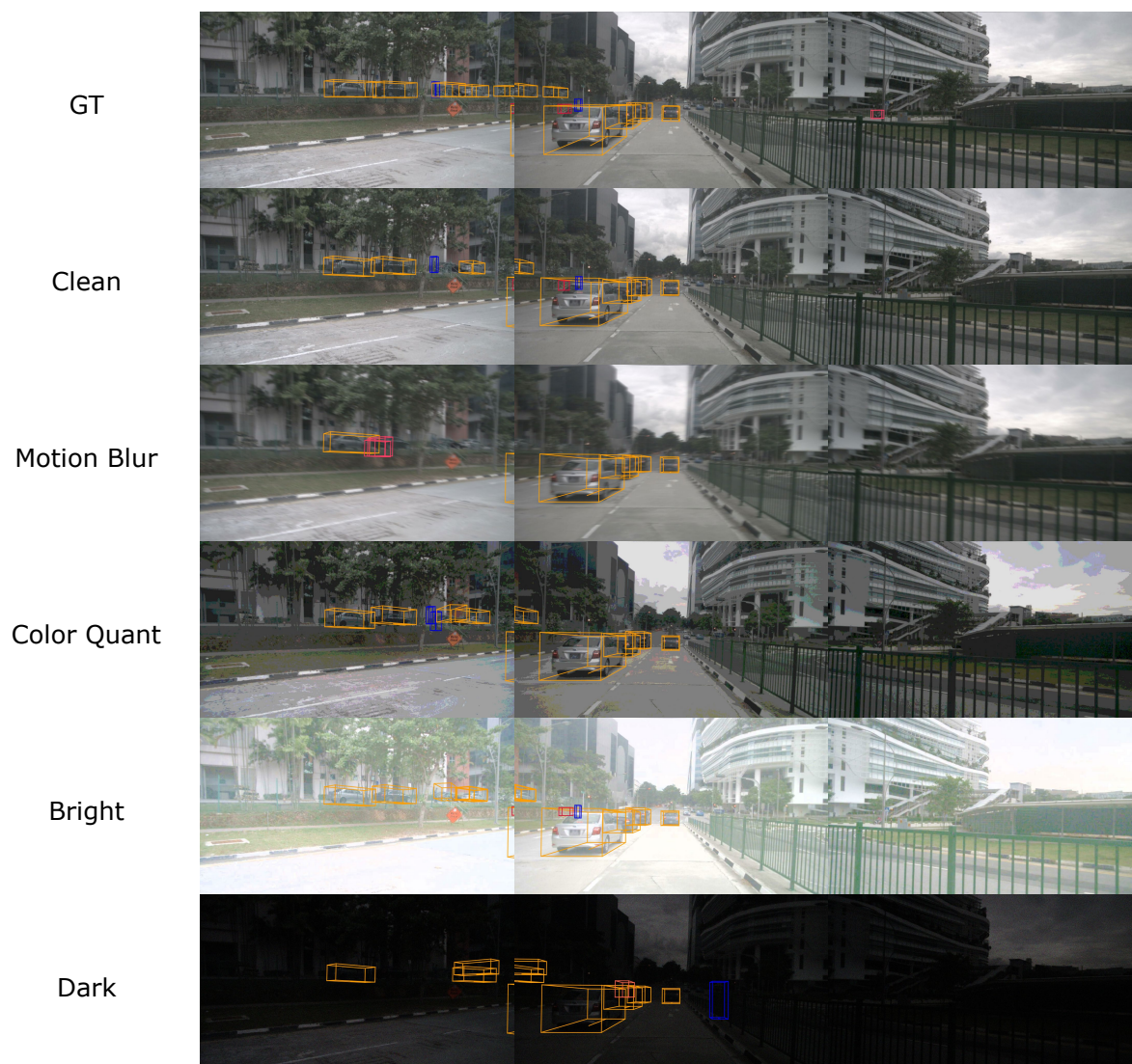


Figure 13. Visualization results of BEVFormer [19] under moderate corruptions.

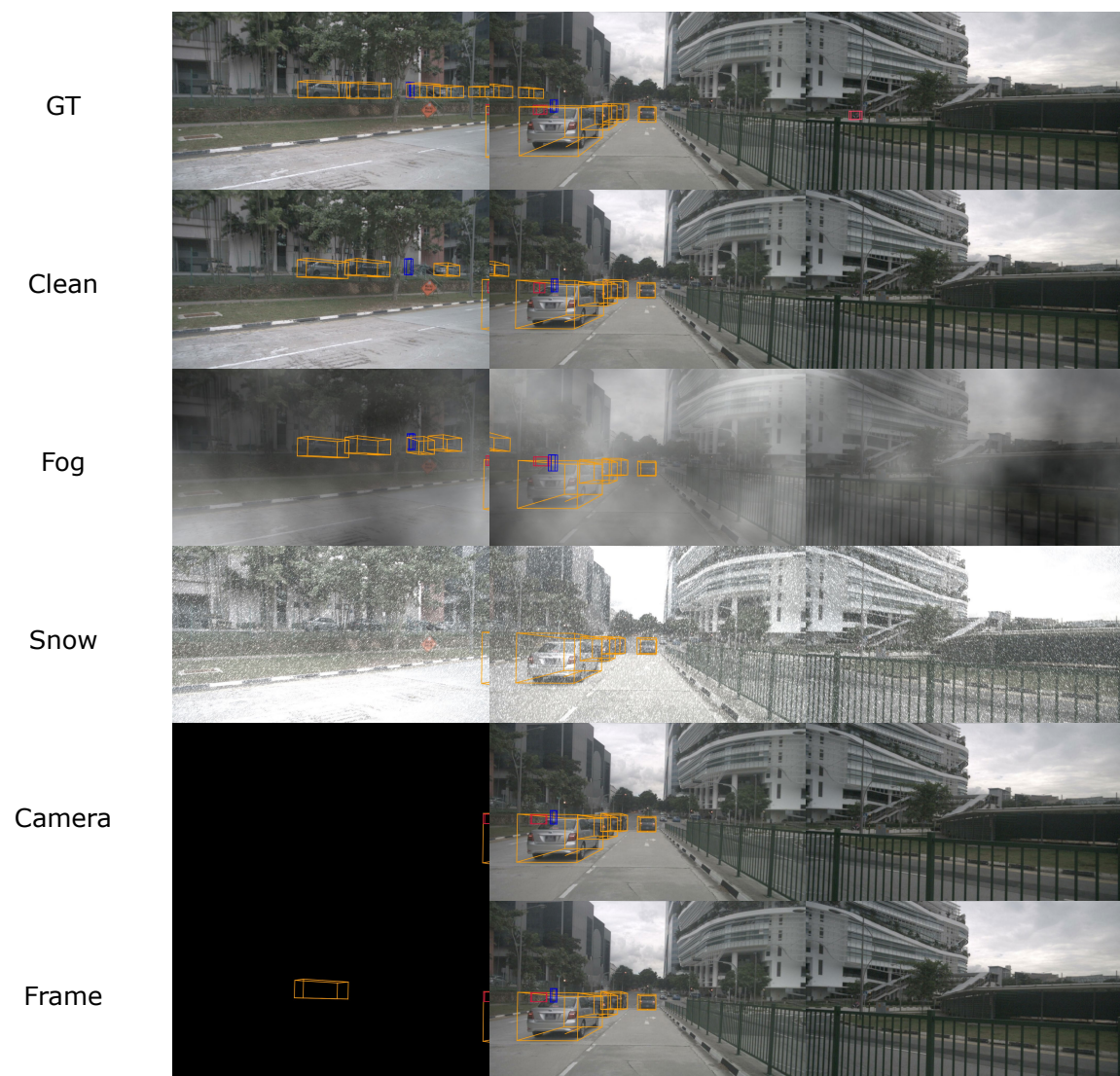


Figure 14. Visualization results of BEVFormer [19] under moderate corruptions.

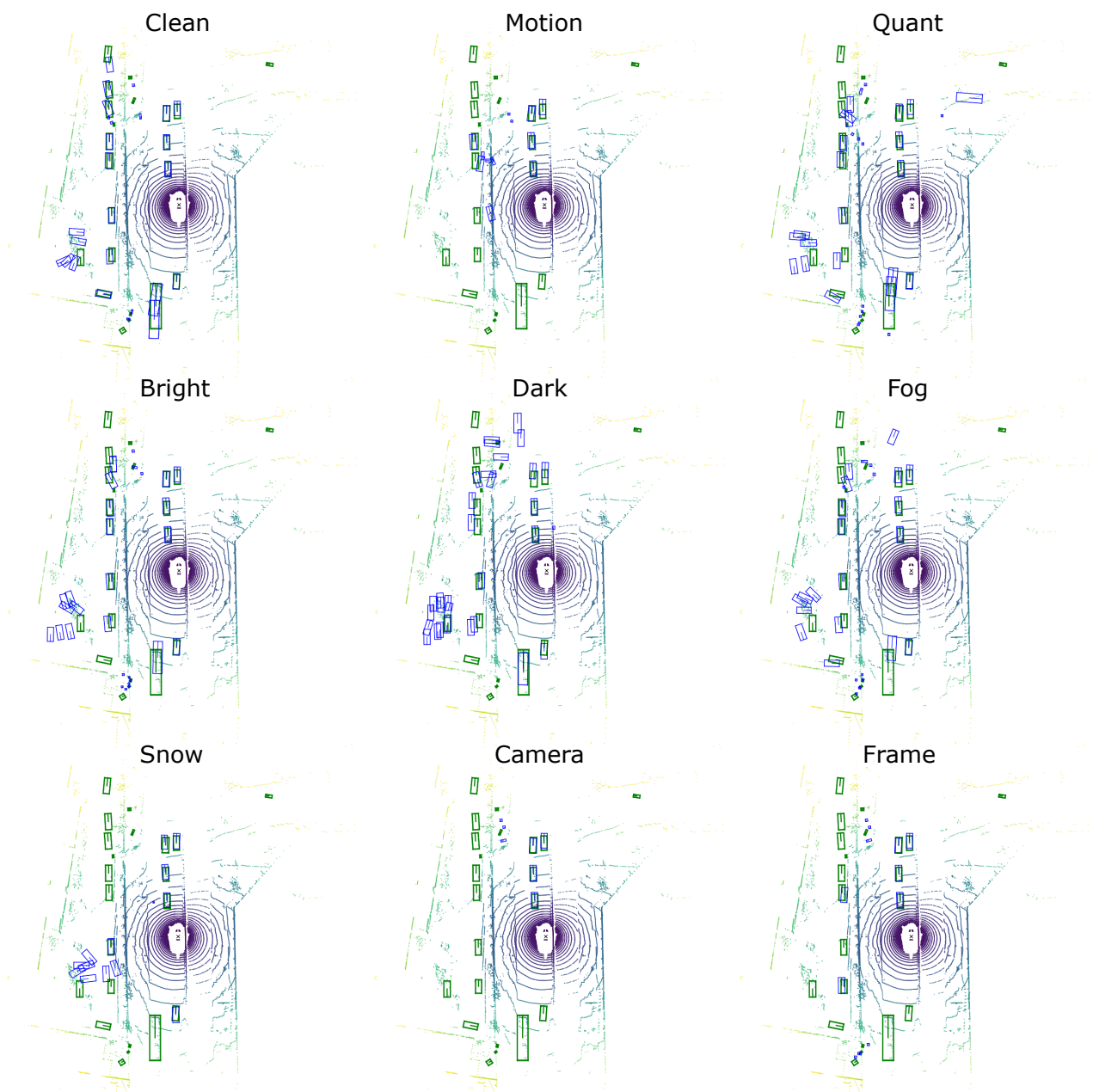


Figure 15. The bird's eye view detection results of BEVFormer [19] under each corruption in the *nuScenes-C* dataset. The green boxes represent ground truth and the blue boxes represent model predictions.

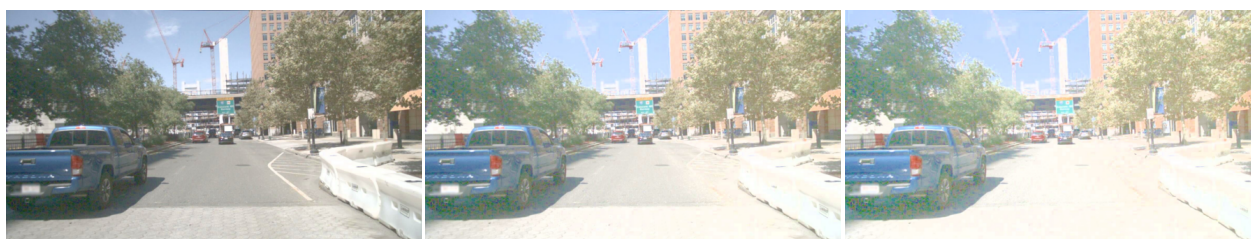
Motion Blur



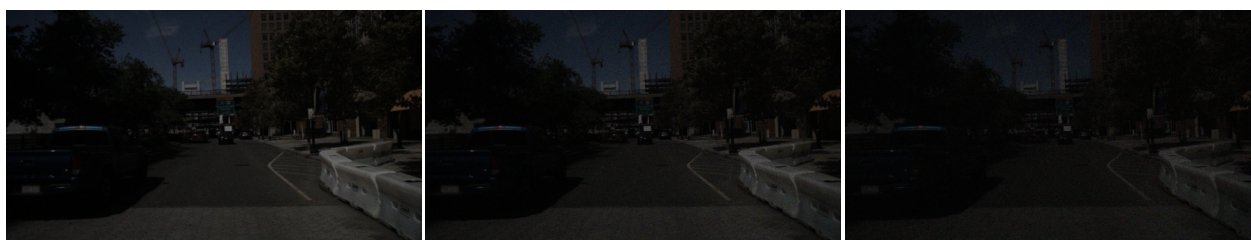
Color Quant



Brightness



Low Light



Fog



Snow



Figure 16. More visualization results of the *nuScenes-C* dataset. Severity levels from left to right: easy, moderate, and hard.

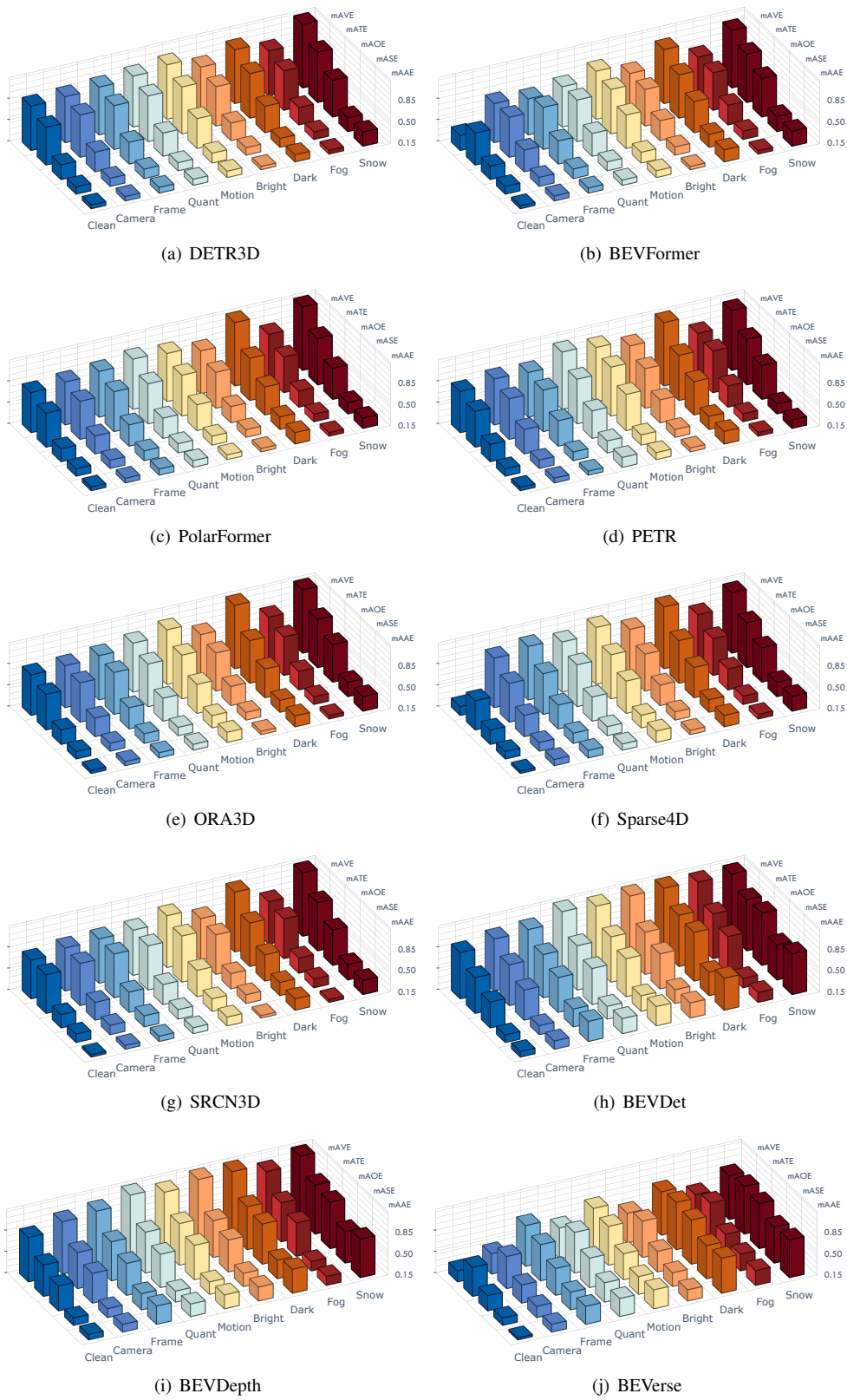


Figure 17. Benchmark results of other metric reported on *nuScenes-C* other than NDS, under different corruption types.

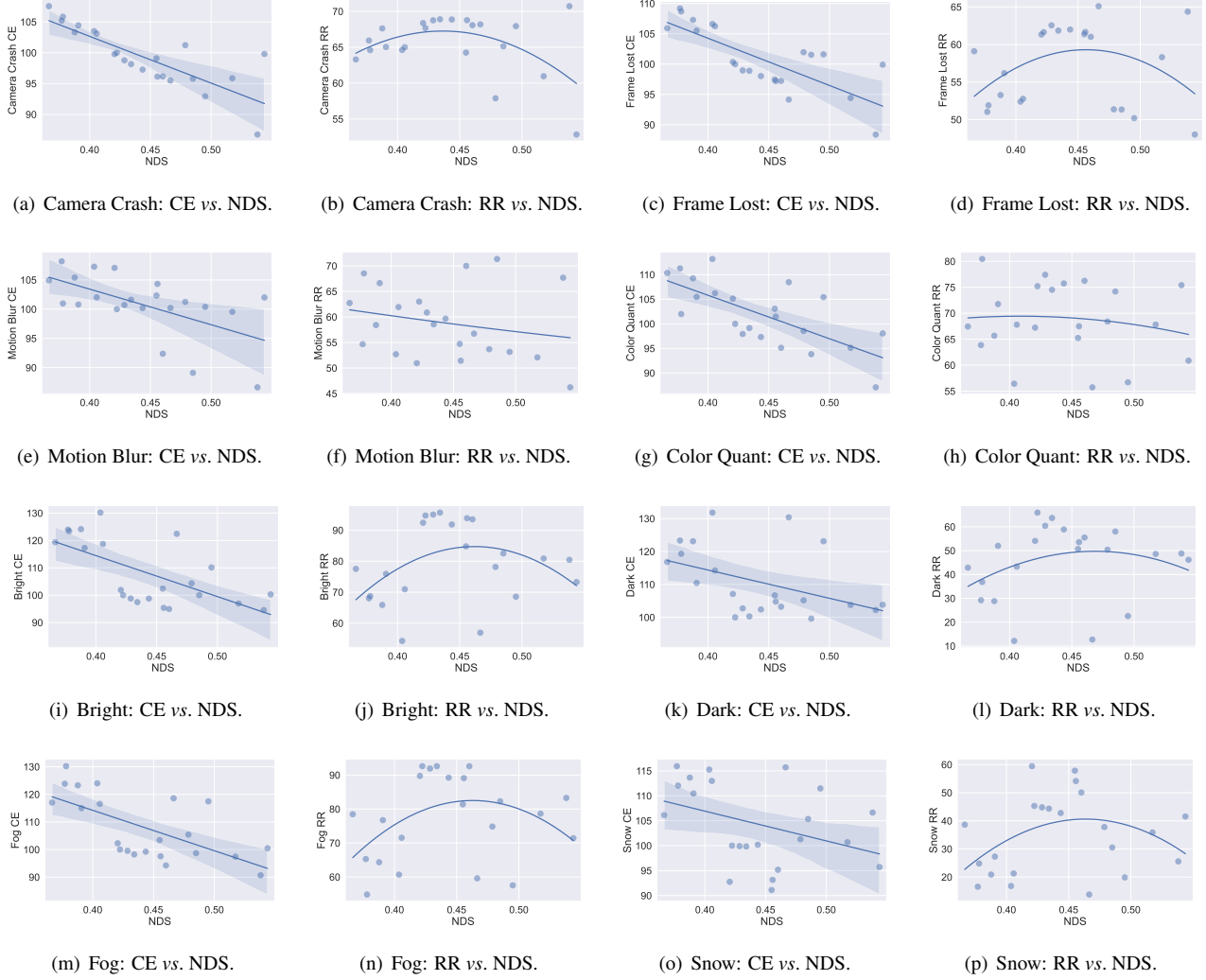


Figure 18. The corruption error (CE) and resilience rate (RR) vs. NDS under each corruption type. It is interesting to notice that the performances follow a strictly linear relationship between the standard dataset and the dataset with temporal corruptions. However, under other semantic corruptions, the robustness does not necessarily show a linear trend, which indicates models' different sensitivities to corruptions.

Corruption	NDS \uparrow	mAP \uparrow	mATE \downarrow	mASE \downarrow	MAOE \downarrow	mAVE \downarrow	mAAE \downarrow
Clean	0.4224	0.3468	0.7647	0.2678	0.3917	0.8754	0.2108
Cam Crash	0.2859	0.1144	0.8400	0.2821	0.4707	0.8992	0.2202
Frame Lost	0.2604	0.0898	0.8647	0.3030	0.5041	0.9297	0.2439
Color Quant	0.3177	0.2165	0.8953	0.2816	0.5266	0.9813	0.2483
Motion Blur	0.2661	0.1479	0.9146	0.3085	0.6351	1.0385	0.2526
Brightness	0.4002	0.3149	0.7915	0.2703	0.4348	0.8733	0.2028
Low Light	0.2786	0.1559	0.8768	0.2947	0.5802	1.0290	0.2654
Fog	0.3912	0.3007	0.7961	0.2711	0.4326	0.8807	0.2110
Snow	0.1913	0.0776	0.9714	0.3752	0.7486	1.2478	0.3797

Table 7. DETR3D [43] results.

Corruption	NDS \uparrow	mAP \uparrow	mATE \downarrow	mASE \downarrow	MAOE \downarrow	mAVE \downarrow	mAAE \downarrow
Clean	0.4341	0.3494	0.7163	0.2682	0.3798	0.8421	0.1997
Cam Crash	0.2991	0.1174	0.7932	0.2853	0.4575	0.8471	0.2131
Frame Lost	0.2685	0.0923	0.8268	0.3135	0.5042	0.8867	0.2455
Color Quant	0.3235	0.2152	0.8571	0.2875	0.5350	0.9354	0.2400
Motion Blur	0.2542	0.1385	0.8909	0.3355	0.6707	1.0682	0.2928
Brightness	0.4154	0.3200	0.7357	0.2720	0.4086	0.8302	0.1990
Low Light	0.2766	0.1539	0.8419	0.3262	0.5682	1.09520	0.2847
Fog	0.4020	0.3012	0.7552	0.2710	0.4237	0.8302	0.2054
Snow	0.1925	0.0702	0.9246	0.3793	0.7648	1.2585	0.3577

Table 8. DETR3D_{CBGS} [43] results.

Corruption	NDS \uparrow	mAP \uparrow	mATE \downarrow	mASE \downarrow	MAOE \downarrow	mAVE \downarrow	mAAE \downarrow
Clean	0.4787	0.3700	0.7212	0.2792	0.4065	0.4364	0.2201
Cam Crash	0.2771	0.1130	0.8627	0.3099	0.5398	0.8376	0.2446
Frame Lost	0.2459	0.0933	0.8959	0.3411	0.5742	0.9154	0.2804
Color Quant	0.3275	0.2109	0.8476	0.2943	0.5234	0.8539	0.2601
Motion Blur	0.2570	0.1344	0.8995	0.3264	0.6774	0.9625	0.2605
Brightness	0.3741	0.2697	0.8064	0.2830	0.4796	0.8162	0.2226
Low Light	0.2413	0.1191	0.8838	0.3598	0.6470	1.0391	0.3323
Fog	0.3583	0.2486	0.8131	0.2862	0.5056	0.8301	0.2251
Snow	0.1809	0.0635	0.9630	0.3855	0.7741	1.1002	0.3863

Table 9. BEVFormer (small) [19] results.

Corruption	NDS \uparrow	mAP \uparrow	mATE \downarrow	mASE \downarrow	MAOE \downarrow	mAVE \downarrow	mAAE \downarrow
Clean	0.2622	0.1324	0.9352	0.3024	0.5556	1.1106	0.2466
Camera Crash	0.2013	0.0425	0.9844	0.3306	0.6330	1.0969	0.2556
Frame Lost	0.1638	0.0292	1.0051	0.4294	0.6963	1.1418	0.3954
Color Quant	0.2313	0.1041	0.9625	0.3131	0.6435	1.1686	0.2882
Motion Blur	0.1916	0.0676	0.9741	0.3644	0.7525	1.3062	0.3307
Brightness	0.2520	0.1250	0.9484	0.3034	0.6046	1.1318	0.2486
Low Light	0.1868	0.0624	0.9414	0.3984	0.7185	1.3064	0.3859
Fog	0.2442	0.1181	0.9498	0.3055	0.6343	1.1806	0.2592
Snow	0.1414	0.0294	1.0231	0.4242	0.8644	1.3622	0.4444

Table 10. BEVFormer-S (small) [19] results.

Corruption	NDS \uparrow	mAP \uparrow	mATE \downarrow	mASE \downarrow	MAOE \downarrow	MAVE \downarrow	MAAE \downarrow
Clean	0.5174	0.4164	0.6726	0.2734	0.3704	0.3941	0.1974
Cam Crash	0.3154	0.1545	0.8015	0.2975	0.5031	0.7865	0.2301
Frame Lost	0.3017	0.1307	0.8359	0.3053	0.5262	0.7364	0.2328
Color Quant	0.3509	0.2393	0.8294	0.2953	0.5200	0.8079	0.2350
Motion Blur	0.2695	0.1531	0.8739	0.3236	0.6941	0.9334	0.2592
Brightness	0.4184	0.3312	0.7457	0.2832	0.4721	0.7686	0.2024
Low Light	0.2515	0.1394	0.8568	0.3601	0.6571	1.0322	0.3453
Fog	0.4069	0.3141	0.7627	0.2837	0.4711	0.7798	0.2046
Snow	0.1857	0.0739	0.9405	0.3966	0.7806	1.0880	0.3951

Table 11. BEVFormer (base) [19] results.

Corruption	NDS \uparrow	mAP \uparrow	mATE \downarrow	mASE \downarrow	MAOE \downarrow	MAVE \downarrow	MAAE \downarrow
Clean	0.4129	0.3461	0.7549	0.2832	0.4520	0.8917	0.2194
Cam Crash	0.2879	0.1240	0.8041	0.2966	0.5094	0.8986	0.2323
Frame Lost	0.2642	0.0969	0.8352	0.3093	0.5748	0.8861	0.2374
Color Quant	0.3207	0.2243	0.8488	0.2992	0.5422	1.0003	0.2522
Motion Blur	0.2518	0.1434	0.8845	0.3248	0.7179	1.1211	0.2860
Brightness	0.3819	0.3093	0.7761	0.2861	0.4999	0.9466	0.2201
Low Light	0.2381	0.1316	0.8640	0.3602	0.6903	1.2132	0.3622
Fog	0.3662	0.2907	0.7938	0.2870	0.5162	0.9702	0.2254
Snow	0.1793	0.0687	0.9472	0.3954	0.8004	1.2524	0.4078

Table 12. BEVFormer-S (base) [19] results.

Corruption	NDS \uparrow	mAP \uparrow	mATE \downarrow	mASE \downarrow	MAOE \downarrow	MAVE \downarrow	MAAE \downarrow
Clean	0.3665	0.3174	0.8397	0.2796	0.6158	0.9543	0.2326
Cam Crash	0.2320	0.1065	0.9383	0.2975	0.7220	1.0169	0.2585
Frame Lost	0.2166	0.0868	0.9513	0.3041	0.7597	1.0081	0.2629
Color Quant	0.2472	0.1734	0.9121	0.3616	0.7807	1.1634	0.3473
Motion Blur	0.2299	0.1378	0.9587	0.3164	0.8461	1.1190	0.2847
Brightness	0.2841	0.2101	0.9049	0.3080	0.7429	1.0838	0.2552
Low Light	0.1571	0.0685	0.9465	0.4222	0.9201	1.4371	0.4971
Fog	0.2876	0.2161	0.9078	0.2928	0.7492	1.1781	0.2549
Snow	0.1417	0.0582	1.0437	0.4411	1.0177	1.3481	0.4713

Table 13. PETR (r50) [23] results.

Corruption	NDS \uparrow	mAP \uparrow	mATE \downarrow	mASE \downarrow	MAOE \downarrow	MAVE \downarrow	MAAE \downarrow
Clean	0.4550	0.4035	0.7362	0.2710	0.4316	0.8249	0.2039
Cam Crash	0.2924	0.1408	0.8167	0.2854	0.5492	0.9014	0.2267
Frame Lost	0.2792	0.1153	0.8311	0.2909	0.5662	0.8816	0.2144
Color Quant	0.2968	0.2089	0.8818	0.3455	0.5997	1.0875	0.3123
Motion Blur	0.2490	0.1395	0.9521	0.3153	0.7424	1.0353	0.2639
Brightness	0.3858	0.3199	0.7982	0.2779	0.5256	0.9342	0.2112
Low Light	0.2305	0.1221	0.8897	0.3645	0.6960	1.2311	0.3553
Fog	0.3703	0.2815	0.8337	0.2778	0.4982	0.8833	0.2111
Snow	0.2632	0.1653	0.8980	0.3138	0.7034	1.1314	0.2886

Table 14. PETR (vov) [23] results.

Corruption	NDS \uparrow	mAP \uparrow	mATE \downarrow	mASE \downarrow	MAOE \downarrow	MAVE \downarrow	MAAE \downarrow
Clean	0.4602	0.3916	0.7060	0.2718	0.3610	0.8079	0.2093
Cam Crash	0.3133	0.1425	0.7746	0.2840	0.4440	0.8524	0.2250
Frame Lost	0.2808	0.1134	0.8034	0.3093	0.4981	0.8988	0.2498
Color Quant	0.3509	0.2538	0.8059	0.2999	0.4812	0.9724	0.2592
Motion Blur	0.3221	0.2117	0.8196	0.2946	0.5727	0.9379	0.2258
Brightness	0.4304	0.3574	0.7390	0.2738	0.4149	0.8522	0.2032
Low Light	0.2554	0.1393	0.8418	0.3557	0.6087	1.2004	0.3364
Fog	0.4262	0.3518	0.7338	0.2735	0.4143	0.8672	0.2082
Snow	0.2304	0.1058	0.9125	0.3363	0.6592	1.2284	0.3174

Table 15. PolarFormer (r101) [14] results.

Corruption	NDS \uparrow	mAP \uparrow	mATE \downarrow	mASE \downarrow	MAOE \downarrow	MAVE \downarrow	MAAE \downarrow
Clean	0.4558	0.4028	0.7097	0.2690	0.4019	0.8682	0.2072
Cam Crash	0.3135	0.1453	0.7626	0.2815	0.4519	0.8735	0.2216
Frame Lost	0.2811	0.1155	0.8019	0.3015	0.4956	0.9158	0.2512
Color Quant	0.3076	0.2000	0.8846	0.2962	0.5393	1.0044	0.2483
Motion Blur	0.2344	0.1256	0.9392	0.3616	0.6840	1.0992	0.3489
Brightness	0.4280	0.3619	0.7447	0.2696	0.4413	0.8667	0.2065
Low Light	0.2441	0.1361	0.8828	0.3647	0.6506	1.2090	0.3419
Fog	0.4061	0.3349	0.7651	0.2743	0.4487	0.9100	0.2156
Snow	0.2468	0.1384	0.9104	0.3375	0.6427	1.1737	0.3337

Table 16. PolarFormer (vov) [14] results.

Corruption	NDS \uparrow	mAP \uparrow	mATE \downarrow	mASE \downarrow	MAOE \downarrow	MAVE \downarrow	MAAE \downarrow
Clean	0.4436	0.3677	0.7319	0.2698	0.3890	0.8150	0.1975
Cam Crash	0.3055	0.1275	0.7952	0.2803	0.4549	0.8376	0.2145
Frame Lost	0.2750	0.0997	0.8362	0.3075	0.4963	0.8747	0.2340
Color Quant	0.3360	0.2382	0.8479	0.2848	0.5249	0.9516	0.2432
Motion Blur	0.2647	0.1527	0.8656	0.3497	0.6251	1.0433	0.3160
Brightness	0.4075	0.3252	0.7740	0.2741	0.4620	0.8372	0.2029
Low Light	0.2613	0.1509	0.8489	0.3445	0.6207	1.2113	0.3278
Fog	0.3959	0.3084	0.7822	0.2753	0.4515	0.8685	0.2048
Snow	0.1898	0.0757	0.9404	0.3857	0.7665	1.2890	0.3879

Table 17. ORA3D [34] results.

Corruption	NDS \uparrow	mAP \uparrow	mATE \downarrow	mASE \downarrow	MAOE \downarrow	MAVE \downarrow	MAAE \downarrow
Clean	0.3770	0.2987	0.7336	0.2744	0.5713	0.9051	0.2394
Cam Crash	0.2486	0.0990	0.8147	0.2975	0.6402	0.9990	0.2842
Frame Lost	0.1924	0.0781	0.8545	0.4413	0.7179	1.0247	0.4780
Color Quant	0.2408	0.1542	0.8718	0.3579	0.7376	1.2194	0.3958
Motion Blur	0.2061	0.1156	0.8891	0.4020	0.7693	1.1521	0.4645
Brightness	0.2565	0.1787	0.8380	0.3736	0.7216	1.2912	0.3955
Low Light	0.1102	0.0470	0.9867	0.5308	0.9443	1.2841	0.6708
Fog	0.2461	0.1404	0.8801	0.3018	0.7483	1.1610	0.3112
Snow	0.0625	0.0254	0.9853	0.7204	1.0029	1.1642	0.8160

Table 18. BEVDet (r50) [13] results.

Corruption	NDS \uparrow	mAP \uparrow	mATE \downarrow	mASE \downarrow	MAOE \downarrow	MAVE \downarrow	MAAE \downarrow
Clean	0.3877	0.3008	0.7035	0.2752	0.5384	0.8715	0.2379
Cam Crash	0.2622	0.1042	0.7821	0.3004	0.6028	0.9783	0.2715
Frame Lost	0.2065	0.0805	0.8248	0.4175	0.6754	1.0578	0.4474
Color Quant	0.2546	0.1566	0.8457	0.3361	0.6966	1.1529	0.3716
Motion Blur	0.2265	0.1278	0.8596	0.3785	0.7112	1.1344	0.4246
Brightness	0.2554	0.1738	0.8094	0.3770	0.7228	1.3752	0.4060
Low Light	0.1118	0.0426	0.9659	0.5550	0.8904	1.3003	0.6836
Fog	0.2495	0.1412	0.8460	0.3269	0.7007	1.1480	0.3376
Snow	0.0810	0.0296	0.9727	0.6758	0.9027	1.1803	0.7869

Table 19. BEVDet (r101) [13] results.

Corruption	NDS \uparrow	mAP \uparrow	mATE \downarrow	mASE \downarrow	MAOE \downarrow	MAVE \downarrow	MAAE \downarrow
Clean	0.3780	0.2846	0.7274	0.2796	0.5517	0.8581	0.2264
Cam Crash	0.2442	0.0928	0.8020	0.3384	0.5815	1.0285	0.3453
Frame Lost	0.1962	0.0720	0.8320	0.4427	0.6830	1.0063	0.4684
Color Quant	0.3041	0.2064	0.7815	0.3247	0.6251	0.9955	0.3212
Motion Blur	0.2590	0.1512	0.7826	0.3675	0.6412	1.1481	0.3973
Brightness	0.2599	0.1714	0.7910	0.3963	0.6828	1.1539	0.4242
Low Light	0.1393	0.0613	0.8761	0.5631	0.8235	1.1739	0.6510
Fog	0.2073	0.0984	0.8521	0.4107	0.6897	1.2659	0.4668
Snow	0.0939	0.0301	0.9494	0.6685	0.8397	1.2412	0.7535

Table 20. BEVDet (r101) FCOS3D pre-trained [13] results.

Corruption	NDS \uparrow	mAP \uparrow	mATE \downarrow	mASE \downarrow	MAOE \downarrow	MAVE \downarrow	MAAE \downarrow
Clean	0.4037	0.3080	0.6648	0.2729	0.5323	0.8278	0.2050
Cam Crash	0.2609	0.1053	0.7786	0.3246	0.5761	0.9821	0.2822
Frame Lost	0.2115	0.0826	0.8174	0.4207	0.6710	1.0138	0.4294
Color Quant	0.2278	0.1487	0.8236	0.4518	0.7461	1.1668	0.4742
Motion Blur	0.2128	0.1235	0.8455	0.4457	0.7074	1.1857	0.5080
Brightness	0.2191	0.1370	0.8300	0.4523	0.7277	1.2995	0.4833
Low Light	0.0490	0.0180	0.9883	0.7696	1.0083	1.1225	0.8607
Fog	0.2450	0.1396	0.8459	0.3656	0.6839	1.2694	0.3520
Snow	0.0680	0.0312	0.9730	0.7665	0.8973	1.2609	0.8393

Table 21. BEVDet (swin-tiny) [13] results.

Corruption	NDS \uparrow	mAP \uparrow	mATE \downarrow	mASE \downarrow	MAOE \downarrow	MAVE \downarrow	MAAE \downarrow
Clean	0.4058	0.3328	0.6633	0.2714	0.5581	0.8763	0.2369
Cam Crash	0.2638	0.1111	0.7407	0.2959	0.6373	1.0079	0.2749
Frame Lost	0.2141	0.0876	0.7890	0.4134	0.6728	1.0536	0.4498
Color Quant	0.2751	0.1865	0.8190	0.3292	0.6946	1.2008	0.3552
Motion Blur	0.2513	0.1508	0.8320	0.3516	0.7135	1.1084	0.3765
Brightness	0.2879	0.2090	0.7520	0.3646	0.6724	1.2089	0.3766
Low Light	0.1757	0.0820	0.8540	0.4509	0.8073	1.3149	0.5410
Fog	0.2903	0.1973	0.7900	0.3021	0.6973	1.0640	0.2940
Snow	0.0863	0.0350	0.9529	0.6682	0.9107	1.2750	0.7802

Table 22. BEVDepth (r50) [18] results.

Corruption	NDS \uparrow	mAP \uparrow	mATE \downarrow	mASE \downarrow	MAOE \downarrow	MAVE \downarrow	MAAE \downarrow
Clean	0.4665	0.3214	0.6807	0.2782	0.4657	0.3281	0.1893
Cam Crash	0.3181	0.1218	0.7447	0.3545	0.5479	0.4974	0.2833
Frame Lost	0.3037	0.1466	0.7892	0.3511	0.6217	0.6491	0.2844
Color Quant	0.2600	0.1497	0.8577	0.4758	0.6711	0.6931	0.4676
Motion Blur	0.2647	0.1456	0.8139	0.4269	0.6275	0.8103	0.4225
Brightness	0.2656	0.1512	0.8120	0.4548	0.6799	0.7029	0.4507
Low Light	0.0593	0.0235	0.9744	0.7926	0.9961	0.9437	0.8304
Fog	0.2781	0.1348	0.8467	0.3967	0.6135	0.6596	0.3764
Snow	0.0644	0.0251	0.9662	0.7966	0.8893	0.9829	0.8464

Table 23. BEVerse (tiny) [47] results.

Corruption	NDS \uparrow	mAP \uparrow	mATE \downarrow	mASE \downarrow	MAOE \downarrow	MAVE \downarrow	MAAE \downarrow
Clean	0.1603	0.0826	0.8298	0.5296	0.8771	1.2639	0.5739
Cam Crash	0.0639	0.0165	0.9135	0.7574	0.9522	1.1890	0.8201
Frame Lost	0.0508	0.0141	0.9455	0.8181	0.9221	1.1765	0.8765
Color Quant	0.0642	0.0317	0.9478	0.7735	0.9723	1.2508	0.8397
Motion Blur	0.0540	0.0230	0.9556	0.8028	0.9339	1.2137	0.8826
Brightness	0.0683	0.0360	0.9369	0.7315	0.9878	1.3048	0.8531
Low Light	0.0100	0.0005	1.0097	0.9474	1.0048	1.1073	0.9561
Fog	0.0402	0.0179	0.9789	0.8230	1.0094	1.3083	0.8962
Snow	0.0107	0.0017	1.0021	0.9468	0.9968	1.1652	0.9612

Table 24. BEVerse-SingleFrame (tiny) [47] results.

Corruption	NDS \uparrow	mAP \uparrow	mATE \downarrow	mASE \downarrow	MAOE \downarrow	MAVE \downarrow	MAAE \downarrow
Clean	0.4951	0.3512	0.6243	0.2694	0.3999	0.3292	0.1827
Cam Crash	0.3364	0.1156	0.6753	0.3331	0.4460	0.4823	0.2772
Frame Lost	0.2485	0.0959	0.7413	0.4389	0.5898	0.8170	0.4445
Color Quant	0.2807	0.1630	0.8148	0.4651	0.6311	0.6511	0.4455
Motion Blur	0.2632	0.1455	0.7866	0.4399	0.5753	0.8424	0.4586
Brightness	0.3394	0.1935	0.7441	0.3736	0.4873	0.6357	0.3326
Low Light	0.1118	0.0373	0.9230	0.6900	0.8727	0.8600	0.7223
Fog	0.2849	0.1291	0.7858	0.4234	0.5105	0.6852	0.3921
Snow	0.0985	0.0357	0.9309	0.7389	0.8864	0.8695	0.7676

Table 25. BEVerse (small) [47] results.

Corruption	NDS \uparrow	mAP \uparrow	mATE \downarrow	mASE \downarrow	MAOE \downarrow	MAVE \downarrow	MAAE \downarrow
Clean	0.2682	0.1513	0.6631	0.4228	0.5406	1.3996	0.4483
Cam Crash	0.1305	0.0340	0.8028	0.6164	0.7475	1.2273	0.6978
Frame Lost	0.0822	0.0274	0.8755	0.7651	0.8674	1.1223	0.8107
Color Quant	0.1002	0.0495	0.8923	0.7228	0.8517	1.1570	0.7850
Motion Blur	0.0716	0.0370	0.9117	0.7927	0.8818	1.1616	0.8833
Brightness	0.1336	0.0724	0.8340	0.6499	0.8086	1.2874	0.7333
Low Light	0.0132	0.0041	0.9862	0.9356	1.0175	0.9964	0.9707
Fog	0.0910	0.0406	0.8894	0.7200	0.8700	1.0564	0.8140
Snow	0.0116	0.0066	0.9785	0.9385	1.0000	1.0000	1.0000

Table 26. BEVerse-SingleFrame (small) [47] results.

Corruption	NDS \uparrow	mAP \uparrow	mATE \downarrow	mASE \downarrow	MAOE \downarrow	MAVE \downarrow	MAAE \downarrow
Clean	0.4286	0.3373	0.7783	0.2873	0.3665	0.7806	0.1878
Cam Crash	0.2947	0.1172	0.8369	0.3017	0.4403	0.8506	0.2097
Frame Lost	0.2681	0.0924	0.8637	0.3303	0.4798	0.8725	0.2349
Color Quant	0.3318	0.2199	0.8696	0.3041	0.4747	0.8877	0.2458
Motion Blur	0.2609	0.1361	0.9026	0.3524	0.5788	0.9964	0.2927
Brightness	0.4074	0.3133	0.7936	0.2911	0.3974	0.8227	0.1877
Low Light	0.2590	0.1406	0.8586	0.3642	0.5773	1.1257	0.3353
Fog	0.3940	0.2932	0.7993	0.2919	0.3978	0.8428	0.1944
Snow	0.1920	0.0734	0.9372	0.3996	0.7302	1.2366	0.3803

Table 27. SRCN3D (r101) [36] results.

Corruption	NDS \uparrow	mAP \uparrow	mATE \downarrow	mASE \downarrow	MAOE \downarrow	MAVE \downarrow	MAAE \downarrow
Clean	0.4205	0.3475	0.7855	0.2994	0.4099	0.8352	0.2030
Cam Crash	0.2875	0.1252	0.8435	0.3139	0.4879	0.8897	0.2165
Frame Lost	0.2579	0.0982	0.8710	0.3428	0.5324	0.9194	0.2458
Color Quant	0.2827	0.1755	0.9167	0.3443	0.5574	1.0077	0.2747
Motion Blur	0.2143	0.1102	0.9833	0.3966	0.7434	1.1151	0.3500
Brightness	0.3886	0.3086	0.8175	0.3018	0.4660	0.8720	0.2001
Low Light	0.2274	0.1142	0.9192	0.3866	0.6475	1.2095	0.3435
Fog	0.3774	0.2911	0.8227	0.3045	0.4646	0.8864	0.2034
Snow	0.2499	0.1418	0.9299	0.3575	0.6125	1.1351	0.3176

Table 28. SRCN3D (vov) [36] results.

Corruption	NDS \uparrow	mAP \uparrow	mATE \downarrow	mASE \downarrow	MAOE \downarrow	MAVE \downarrow	MAAE \downarrow
Clean	0.5438	0.4409	0.6282	0.2721	0.3853	0.2922	0.1888
Cam Crash	0.2873	0.1319	0.7852	0.2917	0.4989	0.9611	0.2510
Frame Lost	0.2611	0.1050	0.8175	0.3166	0.5404	1.0253	0.2726
Color Quant	0.3310	0.2345	0.8348	0.2956	0.5452	0.9712	0.2496
Motion Blur	0.2514	0.1438	0.8719	0.3553	0.6780	1.0817	0.3347
Brightness	0.3984	0.3296	0.7543	0.2835	0.4844	0.9232	0.2187
Low Light	0.2510	0.1386	0.8501	0.3543	0.6464	1.1621	0.3356
Fog	0.3884	0.3097	0.7552	0.2840	0.4933	0.9087	0.2229
Snow	0.2259	0.1275	0.8860	0.3875	0.7116	1.1418	0.3936

Table 29. Sparse4D [20] results.

Corruption	NDS \uparrow	mAP \uparrow	mATE \downarrow	mASE \downarrow	MAOE \downarrow	MAVE \downarrow	MAAE \downarrow
Clean	0.3907	0.3438	0.6691	0.2809	0.6638	0.8803	0.3180
Cam Crash	0.2541	0.1132	0.7542	0.2848	0.7337	0.9248	0.3273
Frame Lost	0.2195	0.0848	0.8066	0.3285	0.7407	1.0092	0.3785
Color Quant	0.2804	0.2013	0.7790	0.3214	0.7702	0.9825	0.3706
Motion Blur	0.2603	0.1717	0.8145	0.2968	0.8353	0.9831	0.3414
Brightness	0.2966	0.2339	0.7497	0.3258	0.8038	1.0663	0.3433
Low Light	0.2033	0.1138	0.7744	0.3716	0.9146	1.1518	0.4757
Fog	0.2998	0.2260	0.7556	0.2908	0.7761	1.0074	0.3238
Snow	0.1066	0.0427	0.9399	0.5888	0.9026	1.1212	0.7160

Table 30. SOLOFusion (short) [31] results.

Corruption	NDS \uparrow	mAP \uparrow	mATE \downarrow	mASE \downarrow	mAOE \downarrow	mAVE \downarrow	mAAE \downarrow
Clean	0.4850	0.3862	0.6292	0.2840	0.6387	0.3151	0.2141
Cam Crash	0.3159	0.1173	0.7462	0.2938	0.6939	0.4614	0.2327
Frame Lost	0.2490	0.1121	0.7824	0.3529	0.8133	0.8167	0.3249
Color Quant	0.3598	0.2233	0.7704	0.3206	0.7326	0.4266	0.2681
Motion Blur	0.3460	0.1969	0.7765	0.2973	0.7849	0.4262	0.2395
Brightness	0.4002	0.2726	0.7163	0.3113	0.6754	0.4251	0.2328
Low Light	0.2814	0.1301	0.7669	0.3701	0.7913	0.5548	0.3534
Fog	0.3991	0.2570	0.7230	0.2947	0.7084	0.3678	0.2002
Snow	0.1480	0.0590	0.8901	0.5666	0.9179	0.7932	0.6480

Table 31. SOLOFusion (long) [31] results.

Corruption	NDS \uparrow	mAP \uparrow	mATE \downarrow	mASE \downarrow	mAOE \downarrow	mAVE \downarrow	mAAE \downarrow
Clean	0.5381	0.4299	0.5842	0.2747	0.4564	0.2426	0.2103
Cam Crash	0.3806	0.1590	0.6607	0.2773	0.5186	0.3152	0.2176
Frame Lost	0.3464	0.1671	0.7161	0.3042	0.5557	0.5292	0.2668
Color Quant	0.4058	0.2572	0.6910	0.3200	0.6217	0.3434	0.2514
Motion Blur	0.3642	0.2019	0.7191	0.3244	0.6643	0.3834	0.2762
Brightness	0.4329	0.2959	0.6532	0.3238	0.5353	0.3808	0.2577
Low Light	0.2626	0.1237	0.7258	0.4567	0.7598	0.5910	0.4597
Fog	0.4480	0.2923	0.6502	0.2883	0.5496	0.2958	0.1973
Snow	0.1376	0.0561	0.8722	0.6480	0.8219	0.8363	0.7255

Table 32. SOLOFusion [31] results.

Corruption	NDS \uparrow	mAP \uparrow	mATE \downarrow	mASE \downarrow	mAOE \downarrow	mAVE \downarrow	mAAE \downarrow
Clean	0.3949	0.3214	0.7538	0.2603	0.4864	1.3321	0.1574
Cam Crash	0.2849	0.1169	0.7842	0.2693	0.5134	1.2993	0.1684
Frame Lost	0.2479	0.0915	0.7912	0.3521	0.5367	1.3668	0.2989
Color Quant	0.2574	0.1548	0.8851	0.3631	0.6378	1.3906	0.3157
Motion Blur	0.2570	0.1459	0.8460	0.3318	0.6894	1.2404	0.2920
Brightness	0.3218	0.2237	0.8243	0.2801	0.6179	1.4902	0.1778
Low Light	0.1468	0.0491	0.8845	0.5287	0.7911	1.3388	0.5729
Fog	0.3321	0.2319	0.8087	0.2702	0.5719	1.2989	0.1879
Snow	0.1136	0.0448	0.9656	0.6321	0.7768	1.2827	0.7141

Table 33. FCOS3D [41] results.

References

- [1] Andrei Barbu, David Mayo, Julian Alverio, William Luo, Christopher Wang, Dan Gutfreund, Josh Tenenbaum, and Boris Katz. Objectnet: A large-scale bias-controlled dataset for pushing the limits of object recognition models. *Advances in Neural Information Processing Systems*, 32, 2019. 3
- [2] Tom B Brown, Dandelion Mané, Aurko Roy, Martín Abadi, and Justin Gilmer. Adversarial patch. *arXiv preprint arXiv:1712.09665*, 2017. 3
- [3] Holger Caesar, Varun Bankiti, Alex H Lang, Sourabh Vora, Venice Erin Liong, Qiang Xu, Anush Krishnan, Yu Pan, Giancarlo Baldan, and Oscar Beijbom. nuscenes: A multi-modal dataset for autonomous driving. In *IEEE/CVF Conference on Computer Vision and Pattern Recognition*, pages 11621–11631, 2020. 1, 3, 4, 5, 10
- [4] Yulong Cao, Ningfei Wang, Chaowei Xiao, Dawei Yang, Jin Fang, Ruigang Yang, Qi Alfred Chen, Mingyan Liu, and Bo Li. Invisible for both camera and lidar: Security of multi-sensor fusion based perception in autonomous driving under physical-world attacks. In *IEEE Symposium on Security and Privacy*, pages 176–194, 2021. 3
- [5] Nicolas Carion, Francisco Massa, Gabriel Synnaeve, Nicolas Usunier, Alexander Kirillov, and Sergey Zagoruyko. End-to-end object detection with transformers. In *European Conference on Computer Vision*, pages 213–229, 2020. 2
- [6] Nicholas Carlini and David Wagner. Towards evaluating the robustness of neural networks. In *IEEE Symposium on Security and Privacy*, pages 39–57, 2017. 1
- [7] MMDetection3D Contributors. MMDetection3D: OpenMMLab next-generation platform for general 3D object detection. <https://github.com/open-mmlab/mmdetection3d>, 2020. 4
- [8] Ian J Goodfellow, Jonathon Shlens, and Christian Szegedy. Explaining and harnessing adversarial examples. *arXiv preprint arXiv:1412.6572*, 2014. 3
- [9] Vitor Guizilini, Rares Ambrus, Sudeep Pillai, Allan Raventos, and Adrien Gaidon. 3d packing for self-supervised monocular depth estimation. In *IEEE/CVF Conference on Computer Vision and Pattern Recognition*, pages 2485–2494, 2020. 7, 10
- [10] Dan Hendrycks, Steven Basart, Norman Mu, Saurav Kadam, Frank Wang, Evan Doro, Rahul Desai, Tyler Zhu, Samyak Parajuli, Mike Guo, et al. The many faces of robustness: A critical analysis of out-of-distribution generalization. In *IEEE/CVF International Conference on Computer Vision*, pages 8340–8349, 2021. 3
- [11] Dan Hendrycks and Thomas Dietterich. Benchmarking neural network robustness to common corruptions and perturbations. *arXiv preprint arXiv:1903.12261*, 2019. 1, 3, 4, 9, 10
- [12] Dan Hendrycks, Kevin Zhao, Steven Basart, Jacob Steinhardt, and Dawn Song. Natural adversarial examples. In *IEEE/CVF Conference on Computer Vision and Pattern Recognition*, pages 15262–15271, 2021. 3
- [13] Junjie Huang, Guan Huang, Zheng Zhu, and Dalong Du. Bevdet: High-performance multi-camera 3d object detection in bird-eye-view. *arXiv preprint arXiv:2112.11790*, 2021. 1, 2, 4, 5, 6, 7, 10, 21, 22
- [14] Yanqin Jiang, Li Zhang, Zhenwei Miao, Xiatian Zhu, Jin Gao, Weiming Hu, and Yu-Gang Jiang. Polarformer: Multi-camera 3d object detection with polar transformers. *arXiv preprint arXiv:2206.15398*, 2022. 3, 4, 5, 6, 8, 10, 21
- [15] Alexey Kurakin, Ian J Goodfellow, and Samy Bengio. Adversarial examples in the physical world. In *Artificial Intelligence Safety and Security*, pages 99–112, 2018. 3
- [16] Alex H Lang, Sourabh Vora, Holger Caesar, Lubing Zhou, Jiong Yang, and Oscar Beijbom. Pointpillars: Fast encoders for object detection from point clouds. In *IEEE/CVF Conference on Computer Vision and Pattern Recognition*, pages 12697–12705, 2019. 1
- [17] Youngwan Lee and Jongyoul Park. Centermask: Real-time anchor-free instance segmentation. In *IEEE/CVF Conference on Computer Vision and Pattern Recognition*, pages 13906–13915, 2020. 7, 8, 9, 10
- [18] Yinhao Li, Zheng Ge, Guanyi Yu, Jinrong Yang, Zengran Wang, Yukang Shi, Jianjian Sun, and Zeming Li. Bevdepth: Acquisition of reliable depth for multi-view 3d object detection. *arXiv preprint arXiv:2206.10092*, 2022. 2, 4, 5, 6, 7, 10, 22
- [19] Zhiqi Li, Wenhao Wang, Hongyang Li, Enze Xie, Chonghao Sima, Tong Lu, Qiao Yu, and Jifeng Dai. Bevformer: Learning bird’s-eye-view representation from multi-camera images via spatiotemporal transformers. In *European Conference on Computer Vision*, pages 1–18, 2022. 1, 3, 4, 5, 6, 7, 8, 9, 10, 13, 14, 15, 19, 20
- [20] Xuewu Lin, Tianwei Lin, Zixiang Pei, Lichao Huang, and Zhizhong Su. Sparse4d: Multi-view 3d object detection with sparse spatial-temporal fusion. *arXiv preprint arXiv:2211.10581*, 2022. 3, 4, 5, 6, 7, 10, 24
- [21] Xin Liu, Huanrui Yang, Ziwei Liu, Linghao Song, Hai Li, and Yiran Chen. Dpatch: An adversarial patch attack on object detectors. *arXiv preprint arXiv:1806.02299*, 2018. 3
- [22] Yanpei Liu, Xinyun Chen, Chang Liu, and Dawn Song. Delving into transferable adversarial examples and black-box attacks. *arXiv preprint arXiv:1611.02770*, 2016. 3
- [23] Yingfei Liu, Tiancai Wang, Xiangyu Zhang, and Jian Sun. Petr: Position embedding transformation for multi-view 3d object detection. *arXiv preprint arXiv:2203.05625*, 2022. 1, 3, 4, 5, 6, 10, 20
- [24] Ze Liu, Yutong Lin, Yue Cao, Han Hu, Yixuan Wei, Zheng Zhang, Stephen Lin, and Baining Guo. Swin transformer: Hierarchical vision transformer using shifted windows. In *IEEE/CVF International Conference on Computer Vision*, pages 10012–10022, 2021. 9
- [25] Zhijian Liu, Haotian Tang, Alexander Amini, Xingyu Yang, Huizi Mao, Daniela Rus, and Song Han. Bevfusion: Multi-task multi-sensor fusion with unified bird’s-eye view representation. In *IEEE International Conference on Robotics and Automation*, 2023. 6, 7
- [26] Yuexin Ma, Tai Wang, Xuyang Bai, Huitong Yang, Yue-nan Hou, Yaming Wang, Yu Qiao, Ruigang Yang, Dinesh Manocha, and Xinge Zhu. Vision-centric bev perception: A survey. *arXiv preprint arXiv:2208.02797*, 2022. 1

- [27] Aleksander Madry, Aleksandar Makelov, Ludwig Schmidt, Dimitris Tsipras, and Adrian Vladu. Towards deep learning models resistant to adversarial attacks. *arXiv preprint arXiv:1706.06083*, 2017. [3](#)
- [28] Seyed-Mohsen Moosavi-Dezfooli, Alhussein Fawzi, Omar Fawzi, and Pascal Frossard. Universal adversarial perturbations. In *IEEE/CVF Conference on Computer Vision and Pattern Recognition*, pages 1765–1773, 2017. [3](#)
- [29] Bowen Pan, Jiankai Sun, Ho Yin Tiga Leung, Alex Andonian, and Bolei Zhou. Cross-view semantic segmentation for sensing surroundings. *IEEE Robotics and Automation Letters*, 5(3):4867–4873, 2020. [10](#), [11](#)
- [30] Dennis Park, Rares Ambrus, Vitor Guizilini, Jie Li, and Adrien Gaidon. Is pseudo-lidar needed for monocular 3d object detection? In *IEEE/CVF International Conference on Computer Vision*, pages 3142–3152, 2021. [10](#)
- [31] Jinhyung Park, Chenfeng Xu, Shijia Yang, Kurt Keutzer, Kris Kitani, Masayoshi Tomizuka, and Wei Zhan. Time will tell: New outlooks and a baseline for temporal multi-view 3d object detection. *International Conference on Learning Representations*, 2023. [3](#), [4](#), [5](#), [6](#), [7](#), [8](#), [10](#), [24](#), [25](#)
- [32] Jonah Philion and Sanja Fidler. Lift, splat, shoot: Encoding images from arbitrary camera rigs by implicitly unprojecting to 3d. In *European Conference on Computer Vision*, pages 194–210, 2020. [2](#)
- [33] Benjamin Recht, Rebecca Roelofs, Ludwig Schmidt, and Vaishaal Shankar. Do imagenet classifiers generalize to imagenet? In *International Conference on Machine Learning*, pages 5389–5400. PMLR, 2019. [3](#)
- [34] Wonseok Roh, Gyusam Chang, Seokha Moon, Giljoo Nam, Chanyoung Kim, Youngyun Kim, Sangpil Kim, and Jinkyu Kim. Ora3d: Overlap region aware multi-view 3d object detection. *arXiv preprint arXiv:2207.00865*, 2022. [2](#), [4](#), [5](#), [6](#), [10](#), [21](#)
- [35] Giulio Rossolini, Federico Nesti, Gianluca D’Amico, Saasha Nair, Alessandro Biondi, and Giorgio Buttazzo. On the real-world adversarial robustness of real-time semantic segmentation models for autonomous driving. *arXiv preprint arXiv:2201.01850*, 2022. [3](#)
- [36] Yining Shi, Jingyan Shen, Yifan Sun, Yunlong Wang, Jiaxin Li, Shiqi Sun, Kun Jiang, and Diange Yang. Srcn3d: Sparse r-cnn 3d surround-view camera object detection and tracking for autonomous driving. *arXiv preprint arXiv:2206.14451*, 2022. [3](#), [4](#), [5](#), [6](#), [7](#), [8](#), [10](#), [24](#)
- [37] Peize Sun, Rufeng Zhang, Yi Jiang, Tao Kong, Chenfeng Xu, Wei Zhan, Masayoshi Tomizuka, Lei Li, Zehuan Yuan, Changhu Wang, et al. Sparse r-cnn: End-to-end object detection with learnable proposals. In *IEEE/CVF Conference on Computer Vision and Pattern Recognition*, pages 14454–14463, 2021. [3](#)
- [38] Christian Szegedy, Wojciech Zaremba, Ilya Sutskever, Joan Bruna, Dumitru Erhan, Ian Goodfellow, and Rob Fergus. Intriguing properties of neural networks. *arXiv preprint arXiv:1312.6199*, 2013. [3](#)
- [39] James Tu, Mengye Ren, Sivabalan Manivasagam, Ming Liang, Bin Yang, Richard Du, Frank Cheng, and Raquel Urtasun. Physically realizable adversarial examples for lidar object detection. In *IEEE/CVF Conference on Computer Vision and Pattern Recognition*, pages 13716–13725, 2020. [3](#)
- [40] Sourabh Vora, Alex H Lang, Bassam Helou, and Oscar Beijbom. Pointpainting: Sequential fusion for 3d object detection. In *IEEE/CVF Conference on Computer Vision and Pattern Recognition*, pages 4604–4612, 2020. [1](#)
- [41] Tai Wang, Xinge Zhu, Jiangmiao Pang, and Dahua Lin. Fcos3d: Fully convolutional one-stage monocular 3d object detection. In *IEEE/CVF International Conference on Computer Vision*, pages 913–922, 2021. [1](#), [4](#), [6](#), [7](#), [10](#), [25](#)
- [42] Tai Wang, Xinge Zhu, Jiangmiao Pang, and Dahua Lin. Probabilistic and geometric depth: Detecting objects in perspective. In *Conference on Robot Learning*, pages 1475–1485. PMLR, 2022. [1](#)
- [43] Yue Wang, Vitor Campagnolo Guizilini, Tianyuan Zhang, Yilun Wang, Hang Zhao, and Justin Solomon. Detr3d: 3d object detection from multi-view images via 3d-to-2d queries. In *Conference on Robot Learning*, pages 180–191. PMLR, 2022. [1](#), [2](#), [4](#), [5](#), [6](#), [7](#), [10](#), [19](#)
- [44] Cihang Xie, Jianyu Wang, Zhishuai Zhang, Yuyin Zhou, Lingxi Xie, and Alan Yuille. Adversarial examples for semantic segmentation and object detection. In *IEEE/CVF International Conference on Computer Vision*, pages 1369–1378, 2017. [3](#)
- [45] Shaoyuan Xie, Zichao Li, Zeyu Wang, and Cihang Xie. On the adversarial robustness of camera-based 3d object detection. *arXiv preprint arXiv:2301.10766*, 2023. [2](#), [3](#)
- [46] Yan Yan, Yuxing Mao, and Bo Li. Second: Sparsely embedded convolutional detection. *Sensors*, 18(10):3337, 2018. [1](#)
- [47] Yunpeng Zhang, Zheng Zhu, Wenzhao Zheng, Junjie Huang, Guan Huang, Jie Zhou, and Jiwen Lu. Beverse: Unified perception and prediction in birds-eye-view for vision-centric autonomous driving. *arXiv preprint arXiv:2205.09743*, 2022. [2](#), [4](#), [5](#), [6](#), [8](#), [9](#), [10](#), [23](#)
- [48] Yin Zhou and Oncel Tuzel. Voxelnet: End-to-end learning for point cloud based 3d object detection. In *IEEE/CVF Conference on Computer Vision and Pattern Recognition*, pages 4490–4499, 2018. [1](#)
- [49] Benjin Zhu, Zhengkai Jiang, Xiangxin Zhou, Zeming Li, and Gang Yu. Class-balanced grouping and sampling for point cloud 3d object detection. *arXiv preprint arXiv:1908.09492*, 2019. [4](#), [6](#)